



Full Flight Envelope and Trim Map of Flapping-Wing Micro Aerial Vehicles

Taylor S. Clawson* and Silvia Ferrari†
 Cornell University, Ithaca, New York 14853
 E. Farrell Helbling‡ and Robert J. Wood§
 Harvard University, Boston, Massachusetts 02138
 and
 Bo Fu,¶ Andy Ruina,** and Z. Jane Wang††
 Cornell University, Ithaca, New York 14853

<https://doi.org/10.2514/1.G004754>

Controlling agile and complex air-vehicle maneuvers requires knowledge of the full flight envelope and dominant modes of motion. This paper presents a comprehensive approach for determining the full flight envelope and trim map of minimally actuated flapping-wing micro aerial vehicles that are capable of a broad range of coupled longitudinal–lateral–directional aerobatic maneuvers. By this approach, a representative set of realizable set points and trim conditions can be determined from the flight dynamic model, including asymmetric and unstable maneuvers. Data-driven dynamic mode decomposition is used to identify and analyze the dominant modes of motion both in simulations and physical experiments involving the RoboBee. The dominant eigenplanes and stability characteristics of this flapping-wing robot are successfully validated experimentally for both stable and unstable asymmetric full-envelope maneuvers, including rapidly uncontrolled tumbling.

Nomenclature

A	= wing attachment point
\mathbf{A}	= state-space matrix
\mathbf{a}	= acceleration vector
\mathbf{B}	= control input matrix
C_D	= drag coefficient
C_{D0}, C_{D1}, C_{L0}	= aerodynamic drag parameters
C_L	= lift coefficient
c	= chord length
d	= distance between wing attachment point and body center of gravity
$d\mathbf{F}_L$	= differential lift force
dy	= spanwise width of a differential wing element
\mathbf{e}_L	= unit vector in the lift force direction
$\{\mathbf{e}_1^i, \mathbf{e}_2^i, \mathbf{e}_3^i\}$	= orthonormal basis for reference frame i
$\mathcal{F}_f, \mathcal{F}_b, \mathcal{F}_l, \mathcal{F}_r$	= inertial, body-fixed, left-wing, and right-wing reference frames
$\mathbf{F}_L, \mathbf{F}_D$	= lift and drag forces
$\mathbf{F}_l, \mathbf{F}_r$	= total aerodynamic forces on the left and right wings
f_l, f_r	= left- and right-wing forcing functions
G	= body center of gravity

\mathbf{g}	= acceleration due to gravity
\mathbf{I}	= rigid-body inertial matrix about center of gravity
k_w	= torsional wing hinge spring constant
L	= left-wing center of gravity
\mathbf{M}	= mass matrix
\mathbf{M}_k	= torsional hinge spring moment
\mathbf{M}_{rd}	= rotational damping moment
m, m_l, m_r	= masses of the robot body, left wing, and right wing
N	= stroke-plane deviation angle shape parameter
$\mathbf{n}_a, \mathbf{n}_o$	= normal vectors to the lateral and longitudinal eigenplanes, calculated from the model
$\tilde{\mathbf{n}}_a, \tilde{\mathbf{n}}_o$	= normal vectors to the lateral and longitudinal eigenplanes, calculated from experimental data
P_l, P_r	= left- and right-wing centers of pressure
p	= \mathbf{e}_1^b component of the body angular rate
\mathbf{p}	= robot physical parameters
q	= \mathbf{e}_2^b component of the body angular rate
\mathbf{q}	= generalized coordinate vector
R	= right-wing center of gravity
r	= \mathbf{e}_3^b component of the body angular rate
\mathbf{r}_A	= position of point A relative to the inertial frame
\mathbf{r}_{AB}	= position of point B relative to point A
\mathbf{r}_G	= position of point G relative to the inertial frame
T	= flapping period
t	= time
t_0	= initial time
U	= trim map
$\mathbf{U}, \Sigma, \mathbf{V}$	= singular value decomposition matrices
u	= \mathbf{e}_1^b component of the body velocity
\mathbf{u}	= robot control input
u_a, u_p, u_y, u_r	= amplitude, pitch, yaw, and roll control inputs
V	= robot airspeed
v	= \mathbf{e}_2^b component of the body velocity
\mathbf{v}	= robot-body velocity
\mathbf{v}_A	= velocity of point A
v_{A_i}	= i th component of the velocity of point A in the wing frame

Received 6 August 2019; revision received 20 February 2020; accepted for publication 26 February 2020; published online Open Access 26 October 2020. Copyright © 2020 by the American Institute of Aeronautics and Astronautics, Inc. All rights reserved. All requests for copying and permission to reprint should be submitted to CCC at www.copyright.com; employ the eISSN 1533-3884 to initiate your request. See also AIAA Rights and Permissions www.aiaa.org/randp.

*Postdoctoral Research Associate, Laboratory for Intelligent Systems and Controls, Sibley School of Mechanical and Aerospace Engineering.

†John Brancaccio Professor and Director, Laboratory for Intelligent Systems and Controls, Sibley School of Mechanical and Aerospace Engineering; ferrari@cornell.edu.

‡Postdoctoral Fellow, Harvard Microrobotics Laboratory, School of Engineering and Applied Sciences.

§Charles River Professor of Engineering and Applied Sciences.

¶Visiting Scientist, Laboratory for Intelligent Systems and Controls, Sibley School of Mechanical and Aerospace Engineering.

**Professor, Sibley School of Mechanical and Aerospace Engineering.

††Professor, Department of Physics and Sibley School of Mechanical and Aerospace Engineering.

$\mathbf{v}_a, \mathbf{v}_o$	=	lateral and longitudinal eigenvectors, calculated from the model
$\tilde{\mathbf{v}}_a, \tilde{\mathbf{v}}_o$	=	lateral and longitudinal eigenvectors, calculated from experimental data
w	=	e_3^b component of the body velocity
x, y, z	=	components of body position in inertial frame
\mathbf{x}	=	state vector
\mathbf{x}_w	=	wing state
Y_{cp}	=	spanwise center of pressure location
\mathbf{y}	=	command vector
Z_{cp}	=	chordwise center of pressure location
α	=	angle of attack
β	=	sideslip angle
γ	=	climb angle
ζ_w	=	wing damping ratio
Θ	=	robot-body orientation
θ	=	roll angle
θ_l, θ_r	=	left- and right-wing stroke-plane deviation angles
$\dot{\xi}$	=	turn rate
ϕ	=	yaw angle
ϕ_l, ϕ_r	=	left- and right-wing stroke angles
ψ	=	pitch angle
ψ_l, ψ_r	=	left- and right-wing pitch angles
$\boldsymbol{\omega}_b$	=	robot-body angular velocity
ω_f	=	flapping-wing forcing frequency
ω_w	=	wing natural frequency
$\nabla(\cdot) _{\mathbf{x}^*, \mathbf{u}^*}$	=	Jacobian matrix evaluated at a set point

I. Introduction

NEW fabrication techniques have enabled the miniaturization of flapping-wing micro aerial vehicles (FWMAVs) equipped with both sensors and actuators at insect scale [1–9]. Besides being lower in cost and allowing access to narrow and confined spaces, these insect-scale robots are safer to operate near people and often survive crash or collisions. As the robot scale decreases, however, many propulsion methods, such as rotating propellers, become increasingly inefficient. Several authors have shown that lower Reynolds numbers and higher losses in the electromagnetic motors cause the reduction in lift-to-drag ratio to become too significant for rotating propellers to work in practice [9,10]. Biologically inspired flapping-wing robots, such as the RoboBee, have become increasingly popular because they are characterized by power-efficient highly maneuverable flight at a record-small size and weight [11,12].

Although many flapping flight controllers have been proposed in the literature [13–24], to date control designs have been demonstrated primarily for hovering regimes and symmetric longitudinal flight [24,25]. The reason is that modeling and analyzing the robot dynamics away from these regimes is made difficult by the nonlinear, periodic, and time-varying nature of asymmetric flapping flight [26]. Moreover, many FWMAV designs are minimally actuated due to stringent size and weight constraints, resulting in passively actuated wing motions and nonminimum phase behaviors. Therefore, although these robots are intrinsically more agile than larger FWMAVs [9], robustly controlled asymmetric aerobatic flapping flight has yet to be successfully demonstrated at this scale. Full-envelope modeling and set-point analysis are at the basis of most conventional fixed-wing or rotary-wing aircraft control systems. In fact, they are key to achieving a systematic understanding and analysis of dominant flight modes and, importantly, they allow the pilot or navigation system to command coupled longitudinal–lateral–directional maneuvers by providing corresponding trim control settings [27–36].

Classic approaches for determining the vehicle flight envelope and set-point mixing logic are not applicable to flapping-wing robots. This is because, away from hovering, state and control variables are time varying and, possibly, periodic even at set-point conditions. Furthermore, propulsion is provided by flapping wings whose motion is constrained by differential equations known as actuator

dynamics. Therefore, establishing the robot flight envelope, normally obtained from available thrust/power curves, instantaneous load factors, and absolute ceiling, requires a fundamentally new method. This paper presents a systematic approach for determining the robot trim map, comprising a set of representative stable and unstable set points (Sec. V), and the flight envelope, representing the physical limitations imposed by the flapping-wing design and kinodynamic constraints (Sec. VI).

Although many flapping-wing flight models have been proposed in the literature [16,23,24,37–49], methods for capturing the robot six-degree-of-freedom dynamics typically assume negligible wing inertia [15,16,39]. Other methods derive new aerodynamic forces and moments that capture unsteady flow effects on the wings by assuming symmetric flapping and pure longitudinal or hovering flight [19,24,25,42,47,50–53]. As a result, many of the existing flight models are not amenable to full flight-envelope calculations or to the analysis of asymmetric flapping and coupled longitudinal–lateral–directional maneuvers, such as steady coordinated turns. For example, stroke-averaged models fail to account for the effects of perturbations in the body configuration on the wing dynamics and, by extension, on the aerodynamic forces on the system [25].

The approach in this paper shows how to obtain the robot full flight envelope and trim map by accounting not only for all of the robot body’s six degrees of freedom (DOFs) but also for the three rotational DOFs of each independent wing. The flight dynamic model incorporates a compact yet effective quasi-steady aerodynamic model originally developed for modeling insect flight [54,55]. All methods are demonstrated using the two-wing minimally actuated insect-scale flapping robot known as RoboBee [56,57]. The same approach is similarly applicable to other popular flapping robots such as the Cox piezoflier [5], the Carnegie Mellon University (CMU) flapping-wing robot [8,58], the U.S. Air Force Research Laboratory piezodriven flapping-wing robot [6], and the designs in Refs. [59–61]. Furthermore, all methods can be easily extended to other flapping-wing configurations characterized by multiple wing pairs [62]; rigid tails [63]; and piezoelectric, electromagnetic, or motor-driven drive actuation [5,8,56–61,63,64]. The full-envelope dynamic model is first validated experimentally for a broad range of RoboBee stable and unstable modes. Then, it is used to analyze the stability of symmetric and asymmetric flapping dominant modes of motion that are identified from the set points both in simulations and physical experiments.

II. Problem Formulation

This paper presents an approach for modeling and analyzing the full-envelope flight dynamics of a broad class of small-scale biologically inspired robots, also known as FWMAVs, that are minimally actuated by pairs of periodically flapping wings attached to a rigid body. The approach is presented and validated using the insect-scale robot known as RoboBee (Fig. 1a) [2], but it can be easily extended to other flapping robots with multiple wing pairs and tails (Fig. 1b), as explained in Sec. III. Many methods have been proposed to date for the modeling and control of flapping-robot dynamics, with standard form

$$\dot{\mathbf{x}}(t) = \mathbf{f}[\mathbf{x}(t), \mathbf{u}(t), \mathbf{p}, t], \quad \mathbf{x}(t_0) = \mathbf{x}_0 \quad (1)$$

where $\mathbf{x} \in \mathbb{R}^n$ is the state, $\mathbf{u} \in \mathbb{R}^m$ is the control input, $\mathbf{p} \in \mathbb{R}^l$ is a vector of parameters, and \mathbf{x}_0 is the initial condition [15–21,23–25,38–41,51,52,65,66]. A key feature that led to some of the first successful FWMAV flights is that the robot is minimally actuated to meet stringent size and weight constraints [26,39]. Although the dynamics are not T periodic, flapping wings are obtained by periodically varying actuation, such as piezoelectric, electromagnetic, or motor-drive mechanisms that control one or more wing states, such as the stroke angle, stroke-plane deviation, and angle of inclination referred to as wing pitch angle in this paper [5,8,56–61,63,64]. In general, the actuator dynamics take the form

$$\mathbf{g}[\dot{\mathbf{x}}_w(t), \mathbf{x}_w(t), \mathbf{u}(t), \mathbf{p}, T, t] = \mathbf{0} \quad (2)$$

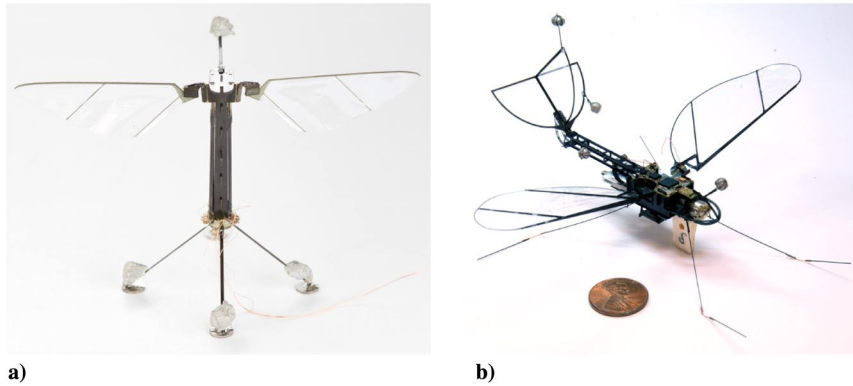


Fig. 1 Photographs of a) minimally actuated FWMAV known as RoboBee and b) example of other robot design characterized by fixed tails and multiple pairs of wings also amenable to the methods presented in this paper.

where $x_w \in \mathbb{R}^s$ is the wing state, and T is the wing-flapping period. For a minimally actuated robot, however, only a small subset of the possible wing states is controlled by the actuators and the remaining ones are passive by design [26,39].

Because of the challenges presented by time-varying underactuated dynamics, the large majority of modeling and control results to date have focused on longitudinal and hovering stable flight, thus limiting our ability to exploit the agility and broad range of behaviors available to these robots, including quasi-steady maneuvers. Full-envelope flight control in fixed-wing aircraft has been achieved over the years by first identifying reduced-order models of dominant modes of motion and, subsequently, by analyzing coupled longitudinal and lateral-directional motions, including quasi-steady asymmetric maneuvers such as coordinated turns [27,30–33,67]. The range of permissible and operational maneuvers defined according to the vehicle's physical limits on airspeed, altitude, and load factor is known as the aircraft *flight envelope*. While the *steady flight envelope* of fixed-wing aircraft can be determined from the curves of thrust/power required and available (Ref. [27] chap. 2), the actual *full flight envelope* is also restricted by other factors, such as stall, absolute ceiling, and instantaneous load factors. Based on the full flight envelope, forward control inputs producing steady and quasi-steady equilibria, known as *set points*, can be determined and used to develop *full-envelope feedback control systems* that are robust and optimal for the full range of maneuvers and behaviors achievable by the robot [27].

Traditionally, a set point (x^*, u^*) is defined by open-loop static or quasi-steady equilibrium conditions corresponding to the desired command vector $y^* \in \mathbb{R}^r$, where

$$y(t) = h[x(t), u(t)] \quad (3)$$

is the system's output equation (Ref. [27] p. 509). The desired command value, y^* , may be provided by a human operator, such as a pilot, or a guidance algorithm. Then, the desired set point (x^*, u^*) can be obtained from dynamic equation (1) by setting selected time derivatives of the state equal to zero. For a quasi-steady equilibrium, one or more of the elements of x^* are integrals of y^* ; therefore, the set point must be determined by computing reduced-order equilibrium conditions. For flapping-wing robots, the state and control variables are typically time varying even at a set point because most of the state elements are T periodic. Therefore, the classic approach for determining the mixing logic that converts desired command values into set points only applies to hovering conditions [26]. Furthermore, fixed-wing aircraft's dominant modes of motion and flight envelope design methods cannot be extended to minimally actuated flapping robots because the thrust/power required and available, as well as all other physical limits on altitude and maneuvering envelope, depend primarily on the wing and actuator design.

This paper presents an approach for analyzing and computing the full flight envelope and set points for the time-varying nonlinear equation of motion [Eq. (1)] and actuator dynamics [Eq. (2)]. It was originally shown in Ref. [33] that, for nonlinear and coupled flight dynamics, the full flight envelope can be obtained from the vehicle

trim map. The trim map represents an inversion of the aircraft nonlinear equation of motion [Eq. (1)] aimed at producing forward control settings u^* that trim the aircraft about a desired maneuver specified by the operator or guidance algorithm via y^* . A subset of trim state elements are directly specified by y^* . The remaining "secondary" values of the state are computed so as not to oppose the maneuver commanded by y^* . The boundary of the trim map constitutes the full flight envelope and provides the limits of the full operational domain, $\mathcal{Y} \subset \mathbb{R}^r$, within which desired commands can be realized by the vehicle. This paper develops a new method for determining the FWMAV trim map:

$$U(p) \triangleq \left\{ u^*: y^* = h(x^*, u^*), x(T) = x^*, \forall y^* \in \mathcal{Y} \right\} \quad (4)$$

and its boundary ∂U numerically from the robot dynamics and output equation. Subsequently, the trim map is used to identify longitudinal and lateral dominant modes of motion and to analyze their stability. Longitudinal, lateral, and coupled modes of motions in asymmetrical flight are all verified experimentally using data-driven dynamic mode decomposition (DMD) [68,69].

III. Full-Envelope FWMAV Dynamic Modeling

Many dynamic models of flapping-wing robots have been proposed to date in the literature. One of the first comprehensive flight dynamic model of minimally actuated flapping robots was developed in Ref. [39] by neglecting the wing inertial effects and by computing the aerodynamic forces and moments by a blade-element approach and cycle averaging. By this approach, a set of six-degree-of-freedom equations of motion analogous to those of rigid-body aircraft were obtained in which the aerodynamic forces and moments consist of periodic functions of time. Later studies developed unsteady nonlinear aerodynamic models applicable in hovering regimes by using unsteady lift empirical formulas able to predict wing effects such as leading-edge vortex [52,53]. Based on these aerodynamic models, the nonlinear flight dynamic equations of hovering FWMAVs were recently obtained in Refs. [24,25] by assuming symmetric flapping, pure longitudinal flight, and constant wing pitch angle through each half-stroke. By this approach, the generalized averaging theory can be applied for analyzing the stability of periodic orbits in hovering and longitudinal regimes. This section presents an approach for deriving and formulating FWMAV kinodynamic equations amenable to full flight envelope and trim-map computation, without imposing prior assumptions on the flight regime or wing-flapping patterns. The approach, presented and validated here for the RoboBee (Fig. 1a) [2], can be easily extended to the aforementioned dynamic models as well as to other minimally actuated robot designs with one or more pairs of flapping wings.

The modeling approach presented in this paper considers the independent motions of each wing (or tail) and the robot body in order to account for the couplings between them, which are shown to play a key role in flapping flight at small scales [70]. The configuration of each

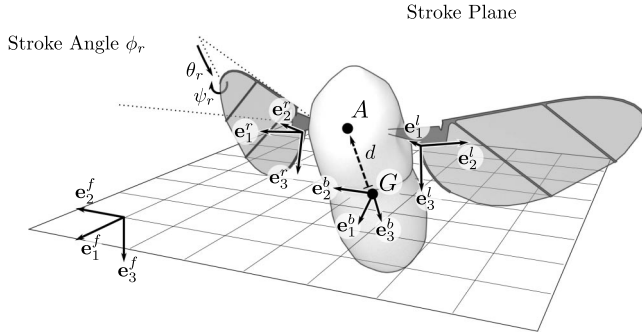


Fig. 2 Orthonormal basis corresponding to body and wing reference frames \mathcal{F}_b , \mathcal{F}_r , and \mathcal{F}_l ; and definition of (right) wing Euler angles ϕ_r , θ_r , and ψ_r .

articulated robot component consists of the position and orientation of a moving frame of reference embedded in the rigid component, as shown in Fig. 2. By this approach, the instantaneous positions and orientations of the robot-body frame \mathcal{F}_b and of the right- and left-wing reference frames (denoted by \mathcal{F}_r and \mathcal{F}_l , respectively) are described relative to an inertial frame of reference \mathcal{F}_f (Fig. 2). Forces and moments generated by each robot component are expressed by adopting an orthonormal basis for each reference frame denoted by set $\{e_1^i, e_2^i, e_3^i\}$, where the superscript i is used to index the body b , the right wing r , and the left wing l . The robot body is modeled as an oblate object $\mathcal{B} \subset \mathbb{R}^3$. The left and right wings are modeled as thin rigid objects $\mathcal{L} \subset \mathbb{R}^3$ and $\mathcal{R} \subset \mathbb{R}^3$, respectively, whose shapes are accounted for by the blade-element approach in Sec. IV. The wings are attached to the robot body at a point A , located at a distance d from the body center of gravity G , measured in the $-\mathbf{e}_3^b$ direction.

The robot translational degrees of freedom are represented by the coordinates of G with respect to the inertial frame \mathcal{F}_f , denoted by x , y , and z . Then, the center-of-gravity position can be represented by the vector $\mathbf{r}_G = xe_1^f + ye_2^f + ze_3^f$, where $\{e_1^f, e_2^f, e_3^f\}$ is the set of orthonormal basis for \mathcal{F}_f . The robot-body and wing orientations are represented by the Euler angles originally proposed in the seminal FWMV work in Refs. [15,39], which differ from those used for conventional fixed-wing aircraft [27]. From Refs. [15,39], the sequence of Euler-angle rotations from the inertial frame to the body frame begins with a rotation about e_3^f by an angle ϕ , followed by a rotation about an inertial axis coincident with the intermediate e_1^b axis by an angle θ , and finally a rotation about e_2^b by an angle ψ . Then, the three rotational degrees of freedom of the robot body are represented by three Euler angles known as yaw ϕ , roll θ , and pitch ψ . The orientation of each wing relative to the body is defined using the nominal stroke plane (Fig. 2), defined as the set of all points $\mathbf{r} \in \mathbb{R}^3$ such that $\mathbf{e}_3^b \cdot (\mathbf{r} - \mathbf{r}_A) = 0$, where \mathbf{r}_A is the inertial position of A with respect to \mathcal{F}_f . As shown in Fig. 2, the orientation of the right wing relative to the body frame \mathcal{F}_b can be represented by three Euler angles known as the stroke angle $\phi_r \in [-\pi, \pi]$, the stroke-plane deviation $\theta_r \in [-\pi, \pi]$, and the wing pitch (or inclination) angle $\psi_r \in [-\pi, \pi]$. The left-wing orientation is similarly defined, except it begins with a rotation about e_3^b by a fixed angle equal to π , such that e_2^l points in the positive spanwise direction of the left wing.

Although, in general the position and orientation of each component in the inertial frame are specified by six variables, the wings' hinge and actuator dynamics (Sec. III.A) constrain the position and orientation of the wings relative to the robot body, respectively, such that the total configuration vector consists of the robot-body position and orientation augmented by the wings' pitch and stroke angles, i.e.,

$$\mathbf{q} = \begin{bmatrix} x & y & z & \phi & \theta & \psi & \phi_r & \psi_r & \phi_l & \psi_l \end{bmatrix}^T \quad (5)$$

body position
body rotation
wing rotation

Furthermore, since the wing stroke angles are constrained by the actuators, the number of degrees of freedom may be reduced from ten to eight.

The robot equations of motion are derived using the Newton–Euler equations for linear and angular momentum balances. The equations are applied to both the robot body and to each flapping wing so as to capture both longitudinal flight and asymmetrical lateral–directional dynamics. Let m denote the mass of the robot body, and let m_l and m_r denote the masses of the left and right wings, respectively. Then, the wing inertia can be accounted for by introducing the influence of gravity \mathbf{g} along with the total aerodynamic forces \mathbf{F}_l and \mathbf{F}_r generated by the left and right wings in nonsymmetric nonhovering nonlongitudinal flight. The blade-element approach previously proposed for insect flight modeling in Ref. [37] is adopted in order to obtain a compact model of significant aerodynamic forces and moments. Although this approach makes several simplifying assumptions, such as neglecting body aerodynamic effects and unsteady flow interactions between the body and the wings, the experimental results in Sec. VIII show that the model adequately captures the aerodynamics of the RoboBee. Other aerodynamic models already available in the literature, including Refs. [53,71], can be similarly adopted and introduced in the flight dynamic model, provided they are first extended to nonlongitudinal nonhovering maneuvers.

Linear momentum balance for the system is written in terms of all gravitational and aerodynamic forces; the linear acceleration of the robot-body center of gravity \mathbf{a}_G ; and the linear accelerations of the centers of gravity of the left and right wings, denoted by \mathbf{a}_L and \mathbf{a}_R respectively, as follows:

$$(m + m_l + m_r)\mathbf{g} + \mathbf{F}_r + \mathbf{F}_l = m\mathbf{a}_G + m_l\mathbf{a}_L + m_r\mathbf{a}_R \quad (6)$$

where the subscripts L and R refer to the centers of gravity of the left and right wings, respectively.

External moments on the system include rotational damping moments of the left and right wings denoted by $\mathbf{M}_{rd,l}$ and $\mathbf{M}_{rd,r}$, respectively. These external moments depend on the positions of the wings' centers of pressure, P_l and P_r , relative to G , denoted by $\mathbf{r}_{GP,l}$ and $\mathbf{r}_{GP,r}$, respectively, and on the positions of the wings' centers of gravity relative to G , denoted by \mathbf{r}_{GL} and \mathbf{r}_{GR} , respectively. Then, the angular momentum balance about G can be written as

$$\mathbf{M}_{rd,l} + \mathbf{r}_{GP,l} \times \mathbf{F}_l + \mathbf{r}_{GL} \times m_l\mathbf{g} + \mathbf{M}_{rd,r} + \mathbf{r}_{GP,r} \times \mathbf{F}_r + \mathbf{r}_{GR} \times m_r\mathbf{g} = \dot{\mathbf{H}}_b + \dot{\mathbf{H}}_l + \dot{\mathbf{H}}_r \quad (7)$$

where $\dot{\mathbf{H}}_b$, $\dot{\mathbf{H}}_l$, and $\dot{\mathbf{H}}_r$ denote the time derivatives of the angular momentum about G of the robot body, left wing, and right wing, respectively. Because G is a noninertial point, the acceleration of each point mass relative to the inertial frame must be accounted for as follows. Let \mathbf{I}_b , \mathbf{I}_l , and \mathbf{I}_r denote the mass moments of inertia of the robot body, left wing, and right wing, respectively, and let the corresponding angular velocities be denoted by $\boldsymbol{\omega}_b$, $\boldsymbol{\omega}_l$, and $\boldsymbol{\omega}_r$. Then, conservation of angular momentum leads to the following equations:

$$\dot{\mathbf{H}}_b = \mathbf{r}_{CG}^{\mathbf{r}0} \times m_b\mathbf{a}_B + \mathbf{I}_b\dot{\boldsymbol{\omega}}_b + \boldsymbol{\omega}_b \times \mathbf{I}_b\boldsymbol{\omega}_b \quad (8)$$

$$\dot{\mathbf{H}}_r = \mathbf{r}_{GR} \times m_r\mathbf{a}_R + \mathbf{I}_r\dot{\boldsymbol{\omega}}_r + \boldsymbol{\omega}_r \times \mathbf{I}_r\boldsymbol{\omega}_r \quad (9)$$

$$\dot{\mathbf{H}}_l = \mathbf{r}_{GL} \times m_l\mathbf{a}_L + \mathbf{I}_l\dot{\boldsymbol{\omega}}_l + \boldsymbol{\omega}_l \times \mathbf{I}_l\boldsymbol{\omega}_l \quad (10)$$

where \mathbf{F}_r , \mathbf{F}_l , $\mathbf{M}_{rd,r}$, and $\mathbf{M}_{rd,l}$ are all significant aerodynamic forces and moments derived using blade-element theory (Sec. IV).

Independent equations for the stroke angles, stroke-plane deviation angles, and wing pitch angles are obtained in order to model the possibly asymmetric motion of the wings. As noted previously, the flight model in this paper assumes no direct control authority over the wing pitch angles. To determine their values, angular momentum balance is computed for each wing about the wing attachment point, A , in the spanwise directions (\mathbf{e}_2^l and \mathbf{e}_2^r):

$$\begin{aligned} \mathbf{e}_2^l \cdot (\mathbf{M}_{rd,l} + \mathbf{r}_{AP,l} \times \mathbf{F}_l + \mathbf{r}_{AL} \times m_l\mathbf{g}) + \mathbf{M}_{k,l} \\ = \mathbf{e}_2^l \cdot (\mathbf{r}_{AL} \times m_l\mathbf{a}_L + \mathbf{I}_l\dot{\boldsymbol{\omega}}_l + \boldsymbol{\omega}_l \times \mathbf{I}_l\boldsymbol{\omega}_l) \end{aligned} \quad (11)$$

$$\begin{aligned} e_2^r \cdot (\mathbf{M}_{rd,r} + \mathbf{r}_{AP_r} \times \mathbf{F}_r + \mathbf{r}_{AR} \times m_r \mathbf{g} + \mathbf{M}_{k,r}) \\ = e_2^l \cdot (\mathbf{r}_{AR} \times m_r \mathbf{a}_R + \mathbf{I}_r \dot{\boldsymbol{\omega}}_r + \boldsymbol{\omega}_r \times \mathbf{I}_r \boldsymbol{\omega}_r) \end{aligned} \quad (12)$$

where \mathbf{r}_{AP_l} and \mathbf{r}_{AP_r} are the position vectors of the wings' centers of pressure relative to A , and \mathbf{r}_{AL} and \mathbf{r}_{AR} are the position vectors of the wings' centers of gravity relative to A . $\mathbf{M}_{k,l} = -k_w \psi_l$ and $\mathbf{M}_{k,r} = -k_w \psi_r$ are the moments caused by torsional springs in the hinges of each wing, characterized by a spring constant k_w . For completeness, all kinematic terms in Eqs. (6–12) are provided in Appendix B.

A. Actuator Dynamics

The precise form of actuator dynamics [Eq. (2)] depends on the design of the wing, the hinge geometry, and the drive mechanism, which may involve piezoelectric, electromagnetic, or motor-driven actuation. As a first step, the control input vector must be determined from the chosen actuation mechanism. In the case of the RoboBee (Fig. 1a), the control drive signals consist of the amplitude input u_a , pitch input u_p , yaw input u_y , and roll input u_r such that

$$\mathbf{u} = [u_a \quad u_p \quad u_y \quad u_r]^T \quad (13)$$

Other drive signals, including those relying on the split-cycle technique in Refs. [16,56,72,73], can be similarly adopted.

In the RoboBee, the robot drive signals affect roll, pitch, and yaw torques by adjusting only the mean stroke angle and stroke amplitude of both wings. In this Raibert-like control method, pitch and roll are controlled similarly to many existing designs, such as in Ref. [56], but yaw torque is controlled by adjusting the mean stroke angle of the right and left wings (RW and LW, respectively) in opposite directions, as shown in Fig. 3. This method generates a yaw torque by affecting the relative phase shift between the pitch angles of the left and right wings [74], as will be shown in Sec. VIII. As a result, the robot flaps at the resonant frequency of the wing and actuator assembly and does

not require wing rotation stops, eliminating unwanted vibrations and increasing overall efficiency [6,75].

The control input directly affects the amplitude and mean offset of the right- and left-wing stroke angles through a forcing function with amplitude u_a . The roll input u_r increases the amplitude of the force on one wing while decreasing the amplitude on the other. The flapping-wing forcing frequency, $\omega_f = 1/T$, is typically chosen to be constant, near the resonant frequency of the actuator assembly for increased efficiency. The pitch input u_p biases the stroke angles symmetrically, and the yaw input u_y biases one stroke angle forward and the other rearward. Biasing the stroke angles in this manner creates a yaw torque, under proper assumptions, as shown in Appendix A. The wing stroke angles (ϕ_r and ϕ_l) are determined entirely by \mathbf{u} and do not depend on any state variables. Previous studies have demonstrated that linear models can capture key aspects of the wing-actuator dynamics without relying excessively on knowledge of hinge-mechanism parameters [7]. Decoupling the stroke angle dynamics from external forces is valid only if the advance ratio, defined as the ratio of the flight speed over the mean wingtip velocity, is less than one. Because the advance ratio typically is less than one, even at maximum flight speed, the wing stroke angles can be assumed governed by second-order linear dynamical systems with lumped parameters ω_w and ζ_w chosen to match the natural frequency and damping ratio of the physical actuators [76], i.e.,

$$\begin{aligned} \ddot{\phi}_{r,l}(t) + 2\zeta_w \omega_w \dot{\phi}_{r,l}(t) + \omega_w^2 \phi_{r,l}(t) \\ = \frac{u_a(t) \pm u_r(t)}{2} \sin(\omega_f t) - u_p(t) \pm u_y(t) \end{aligned} \quad (14)$$

It can be seen that the forcing functions in the actuator dynamics [Eq. (14)], representing the actuator drive signals, are determined solely by the flapping-wing forcing frequency parameter ω_f and the control inputs \mathbf{u} .

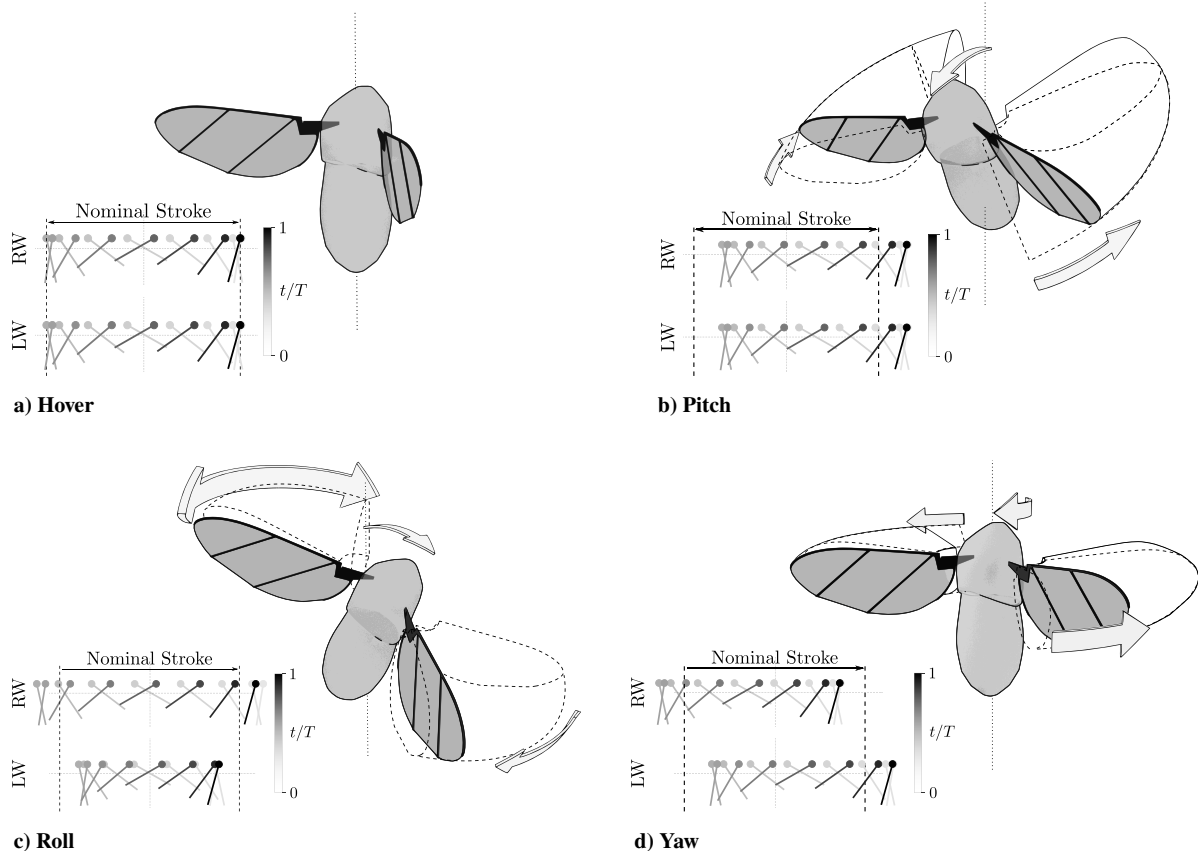


Fig. 3 In addition to a) hovering and b) longitudinal pitch motions, flapping wings with asymmetric wing strokes (bias) achieve lateral-directional control of c) roll and d) yaw motions.

The wing stroke-plane deviation angles are constrained by the geometry of the wing hinge and actuator assembly. In the case of the RoboBee, these constraints can be characterized by the harmonic function originally proposed in Ref. [37]:

$$\theta_{r,i}(t) = \theta_0 + \theta_m \cos(N\omega_f t + \delta_\theta), \quad N = 1, 2 \quad (15)$$

where the nominal offset θ_0 , the deviation amplitude θ_m , and the phase shift δ_θ are robot parameters contained in \mathbf{p} . Also, $N = 1$ when a single vertical oscillation occurs per stroke, and $N = 2$ when the wingtip traces a figure eight. Finally, the wing pitch angles (ψ_r and ψ_l) are passively controlled; thus, they are included in the state vector \mathbf{x} . Therefore, the dynamic constraint [Eq. (14)] and the algebraic constraint [Eq. (15)] together comprise the actuator constraints, which can be cast in standard form [Eq. (2)] by bringing all of the terms to the left-hand side of the equations.

The approach can also be extended to designs with multiple wing pairs and/or tails by introducing constraint equations for the wing and/or tail Euler angles and by expressing them in terms of the control vector \mathbf{u} whenever the angles are actuated. All of the wing Euler angles and their time derivatives are then included in the robot state vector as shown in the next subsection. Aerodynamic interactions between wings may also need to be accounted for in robots with many closely spaced wing pairs.

B. Standard Forms of FWMAV Flight Dynamics

Equations (6–12) together constitute the equations of motion of the robot that are subject to the actuator dynamic constraints [Eqs. (14) and (15)]. They can be cast in standard form [Eq. (1)] by expressing the control inputs in the vector form [Eq. (13)] and by organizing all of the state variables in the vector:

$$\mathbf{x} = [\phi_r \ \psi_r \ \phi_l \ \psi_l \ \dot{\phi}_r \ \dot{\psi}_r \ \dot{\phi}_l \ \dot{\psi}_l \ x \ y \ z \ \phi \ \theta \ \psi \ u \ v \ w \ p \ q \ r]^T \quad (16)$$

where x , y , and z are the inertial coordinates of the body center of gravity G . Also, ϕ , θ , and ψ are the robot-body Euler angles. Note that u , v , and w are the components of the robot velocity in the body frame. Also, p , q , and r are the components of the robot angular rate in the body frame. The complete state of the flapping-wing robot also includes all elements of the wing state vector:

$$\mathbf{x}_w = [\phi_r \ \psi_r \ \phi_l \ \psi_l \ \dot{\phi}_r \ \dot{\psi}_r \ \dot{\phi}_l \ \dot{\psi}_l]^T \quad (17)$$

The masses, moments of inertia, aerodynamic coefficients, center-of-gravity position vectors, and actuator parameters can be organized into the vector \mathbf{p} , which depends solely on the robot design and fabrication and, in this paper, is assumed constant.

Using the generalized configuration coordinates in Eq. (5), it can be easily shown that the equations are linear in $\ddot{\mathbf{q}}$, and can be expressed in terms of the mass matrix $\mathbf{M}(\mathbf{q}) \in \mathbb{R}^{(n/2) \times (n/2)}$, the nonlinear terms $\mathbf{C}(\mathbf{q}, \dot{\mathbf{q}}) \in \mathbb{R}^{(n/2)}$, and the input matrix $\mathbf{B}(t) \in \mathbb{R}^{(n/2) \times m}$ as follows:

$$\mathbf{M}(\mathbf{q})\ddot{\mathbf{q}} + \mathbf{C}(\mathbf{q}, \dot{\mathbf{q}}) = \mathbf{B}(t)\mathbf{u} \quad (18)$$

Solving Eq. (18) for $\ddot{\mathbf{q}}(t)$, an expression is obtained in terms of the state time derivative:

$$\begin{bmatrix} \dot{\mathbf{q}} \\ \ddot{\mathbf{q}} \end{bmatrix} = \begin{bmatrix} \mathbf{0} & \mathbf{I} \\ \mathbf{0} & \mathbf{0} \end{bmatrix} \mathbf{x}(t) - \begin{bmatrix} \mathbf{0} \\ \mathbf{M}(\mathbf{q})^{-1} \mathbf{C}(\mathbf{q}, \dot{\mathbf{q}}) \end{bmatrix} + \begin{bmatrix} \mathbf{0} \\ \mathbf{M}(\mathbf{q})^{-1} \mathbf{B}(t) \end{bmatrix} \mathbf{u}(t) \quad (19)$$

Therefore, it can be seen that the FWMAV dynamics are in the affine form

$$\dot{\mathbf{x}}(t) = \mathbf{f}(\mathbf{x}) + \mathbf{G}(\mathbf{x}, t)\mathbf{u}(t) \quad (20)$$

The precise form of the vector and matrix functions in Eqs. (18) and (20) depends on the aerodynamic forces and moments derived in the next section and is omitted in this paper for brevity.

IV. Blade-Element Calculations of Aerodynamic Forces and Moments

Modeling wing aerodynamic forces for flapping-wing robots is complicated due to the periodic nature of flapping and the presence of unsteady aerodynamic effects caused by the acceleration of the wing during stroke reversal. During flapping, wings periodically experience high angles of attack, stall, and high rates of rotation. Many studies have been performed to better characterize the aerodynamic forces and moments during flight [54,77,78]. Quasi-steady models have been proposed in an effort to approximate the stroke-averaged forces and moments acting on the wings without incurring the high computational costs associated with computational fluid dynamic approaches [39,79,80]. The quasi-steady models adopted in this paper obtain local wing lift and drag forces by considering differential elements of the wing, as shown in Fig. 4, and by integrating the resulting forces over the entire wing surface [54,78].

For simplicity, consider the translational aerodynamic forces and their dependence on the lift and drag coefficients $C_L(\alpha_i)$ and $C_D(\alpha_i)$, each implicit functions of the angle of attack α_i of the left ($i = l$) or right ($i = r$) wing. The equations for the lift and drag coefficients determined from experiments and numerical calculations are

$$C_L(\alpha_i) = C_{L0} \sin(2\alpha_i) \quad (21)$$

$$C_D(\alpha_i) = C_{D0} - C_{D1} \cos(2\alpha_i) \quad (22)$$

as shown in Refs. [54,71]. What follows is the computation of aerodynamic forces and moments for each wing. A point Q is defined to lie in the spanwise center of each differential element on the \mathbf{e}_2^i axis. The angle of attack α_i is defined as the angle between the velocity \mathbf{v}_Q relative to the surrounding fluid and \mathbf{e}_3^i in the plane normal to the spanwise direction of the wing \mathbf{e}_2^i such that

$$\alpha_i = -\arctan\left(\frac{\mathbf{v}_Q^T \mathbf{e}_1^i}{\mathbf{v}_Q^T \mathbf{e}_3^i}\right) \quad (23)$$

The differential lift force acting on a differential wing element is

$$d\mathbf{F}_L = \left(\frac{1}{2}\rho \mathbf{v}_Q^T \mathbf{v}_Q C_L(\alpha_i) c(y) dy\right) \mathbf{e}_L \quad (24)$$

where ρ is the density of the surrounding fluid, $c(y)$ is the chord length of the element, and dy is the spanwise width of the element. The lift force acts in the \mathbf{e}_L direction, which is normal to the relative velocity \mathbf{v} :

$$\mathbf{e}_L = -\cos(\alpha_i)\mathbf{e}_1^i - \sin(\alpha_i)\mathbf{e}_3^i \quad (25)$$

Then, the total lift force acting on the wing can be obtained by integrating Eq. (24) along the wing span:

$$\mathbf{F}_L = \left(\frac{1}{2}\rho C_L(\alpha_i) \int_{y_0}^{y_f} \mathbf{v}_Q^T \mathbf{v}_Q c(y) dy\right) \mathbf{e}_L \quad (26)$$

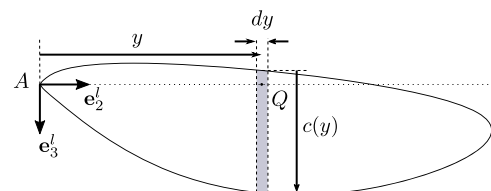


Fig. 4 Two-dimensional view of the left wing showing a single differential blade element used for the calculation of aerodynamic forces on the wing.

The local velocity can also be written as the sum of the velocity \mathbf{v}_A at the hinge point A and the velocity \mathbf{v}_{AQ} of the differential element relative to the hinge such that $\mathbf{v} = \mathbf{v}_A + \mathbf{v}_{AQ}$. Substituting this expression for local velocity into Eq. (26) yields

$$\mathbf{F}_L = \frac{1}{2}\rho C_L(\alpha_i) \left(\mathbf{v}_A^T \mathbf{v}_A \int_{y_0}^{y_f} c(y) dy + \int_{y_0}^{y_f} (2\mathbf{v}_A^T \mathbf{v}_{AQ} + \mathbf{v}_{AQ}^T \mathbf{v}_{AQ}) c(y) dy \right) \mathbf{e}_L \quad (27)$$

where both integrals in Eq. (27) depend on the wing geometry and \mathbf{v}_Q . The preceding expression requires repeated evaluations, and therefore is simplified as follows. Let

$$\mathbf{v}_{A_1} \triangleq \mathbf{v}_A^T \mathbf{e}_1^i$$

denote the wing-frame components of the velocity, and

$$\omega_{w_1} \triangleq \omega_w^T \mathbf{e}_1^i$$

denote the wing-frame components of the wing angular rate. Then, the integrals in Eq. (27) can be decomposed and simplified to

$$\mathbf{F}_L = \frac{1}{2}\rho C_L(\alpha_i) (\mathbf{v}_A^T \mathbf{v}_A C_1 + 2(\mathbf{v}_{A_3} \omega_{w_1} - \mathbf{v}_{A_1} \omega_{w_3}) C_2 + (\omega_{w_1}^2 + \omega_{w_3}^2) C_3) \mathbf{e}_L \quad (28)$$

where

$$C_1 \triangleq \int_{y_0}^{y_f} c(y) dy, \quad C_2 \triangleq \int_{y_0}^{y_f} y c(y) dy, \quad C_3 \triangleq \int_{y_0}^{y_f} y^2 c(y) dy \quad (29)$$

Similarly, the drag is computed as follows:

$$\mathbf{F}_D = \frac{1}{2}\rho C_D(\alpha) (\mathbf{v}_A^T \mathbf{v}_A C_1 + 2(\mathbf{v}_{A_3} \omega_{w_1} - \mathbf{v}_{A_1} \omega_{w_3}) C_2 + (\omega_{w_1}^2 + \omega_{w_3}^2) C_3) \mathbf{e}_D \quad (30)$$

and acts along the direction of the unit vector

$$\mathbf{e}_D = -\sin(\alpha_i) \mathbf{e}_1^i + \cos(\alpha_i) \mathbf{e}_3^i \quad (31)$$

which represents the direction of the velocity of the surrounding fluid relative to the wing. Then, the total aerodynamic force acting on each wing \mathbf{F}_i is given by the sum of the wing lift and drag forces.

The lift and drag forces both can be assumed to act at the wing's center of pressure with position

$$\mathbf{r}_{AP_i} = Y_{cp} \mathbf{e}_2^i + Z_{cp}(\alpha_i) \mathbf{e}_3^i \quad (32)$$

relative to A , where Y_{cp} and Z_{cp} are the spanwise and chordwise locations of the center of pressure, respectively. Previous studies in fruit flies [21] and robotic wings [81] showed that Y_{cp} is relatively constant with respect to changes in angle of attack and that Z_{cp} obeys the empirical relationship

$$Z_{cp}(\alpha_i) = \int_{y_0}^{y_f} c(y) \left(\frac{0.82|\alpha_i|}{\pi} + 0.05 \right) dy \quad (33)$$

Finally, local aerodynamic forces cause rotational damping effects about the spanwise direction of the wing \mathbf{e}_2^i [21,78,81]. The rotational damping moment is found by integrating the local drag on a rectangular differential element of the wing in both the chordwise and spanwise directions:

$$\mathbf{M}_{rd,i} = \left(\frac{1}{2}\rho C_D(\pi/2) \int_{z_0}^{z_1} \int_0^R |\mathbf{v}_Q^T \mathbf{e}_1^i| |\mathbf{v}_Q^T \mathbf{e}_1^i| z dr dz \right) \mathbf{e}_2^i \quad (34)$$

Together, Eqs. (28), (30), (32), and (34) describe the wing aerodynamic forces and moments and the locations of the centers of pressure used in the robot dynamic equations [Eq. (20)]. The RoboBee parameters described in Ref. [56] and the flapping frequency of $\omega_f = (\pi/60)$ rad/s, are adopted in this paper.

V. FWMAV Set-Point Mixing Logic and Trim Map

This section develops a new approach for obtaining the FWMAV mixing logic that converts desired values of the command variable \mathbf{y}^* into a feasible quasi-steady set point $(\mathbf{x}^*, \mathbf{u}^*)$. Because of the periodic nature of flapping flight, existing approaches for computing vehicle set points are not applicable to flapping insect-scale robots. By developing the set-point mixing logic, a trim map can be obtained for the robot, thus establishing the boundaries of the flight envelope based on the nonlinear dynamic and output equations (1–3). Also, the trim map U , defined in Eq. (4), provides a forward controller able to stabilize the robot under ideal conditions. In practice, modeling errors and other uncertainties can be accounted for by augmenting the trim map with a nonzero-set-point regulator that can be written directly in terms of \mathbf{y}^* to provide insight into the partitioning between robust feedback control and steady-state maneuvers (Ref. [28] p. 14), as demonstrated in Refs. [14,26] for longitudinal FWMAV flight.

As a first step, the robot state vector [Eq. (16)] is partitioned into a vector of variables that are T periodic at the set point

$$\mathbf{x}_1^*(t+T) = \mathbf{x}_1^*(t) \quad (35)$$

and a vector of time-varying variables $\mathbf{x}_2^*(t)$ that are not periodic and, typically, are integrals of one or more variables in $\mathbf{x}_1^*(t)$. It is common practice to assume that the flapping period T is the least value for which the equality in Eq. (35) holds; thus, Eq. (35) also holds for any multiples of T . The T -periodic state vector \mathbf{x}_1 includes the wing state [Eq. (17)] so as to allow the flapping robot to maintain quasi-steady maneuvers. For the RoboBee, the T -periodic state is

$$\mathbf{x}_1 = [\mathbf{x}_w^T \quad \theta \quad \psi \quad u \quad v \quad w \quad p \quad q \quad r]^T \quad (36)$$

Therefore, it follows that

$$\mathbf{x}_2 = [x \quad y \quad z \quad \phi]^T \quad (37)$$

The mixing logic that determines the desired state \mathbf{x}^* as a function of the desired command input \mathbf{y}^* is determined from the output equation [Eq. (3)] and the flapping flight dynamic model (Sec. III), as shown in Secs. V.A–V.D. Subsequently, the desired (trim) control settings \mathbf{u}^* are determined numerically from the nonlinear dynamic equation [Eq. (1)]. When a solution for \mathbf{u}^* cannot be obtained, the commanded maneuver exceeds the physical limitations of the robot; thus, it is excluded from its trim map U .

A. Coordinated Flapping Turn

The coordinated turn, illustrated in Fig. 5, is the most general quasi-steady flight maneuver [27]. For flapping-wing flight, a quasi-steady maneuver can be defined as a robot trajectory for which the body-frame components of the linear and angular velocities are T periodic. The geometry and parameters of the coordinated turn can be specified by the command input

$$\mathbf{y} = [V \quad \gamma \quad \dot{\xi} \quad \beta]^T \quad (38)$$

where V is the robot airspeed, γ is the climb angle, β is the sideslip angle, and $\dot{\xi}$ is the turn rate. When the turn rate $\dot{\xi}$ is nonzero, it can be used in conjunction with the commanded forward speed to obtain the robot turn radius

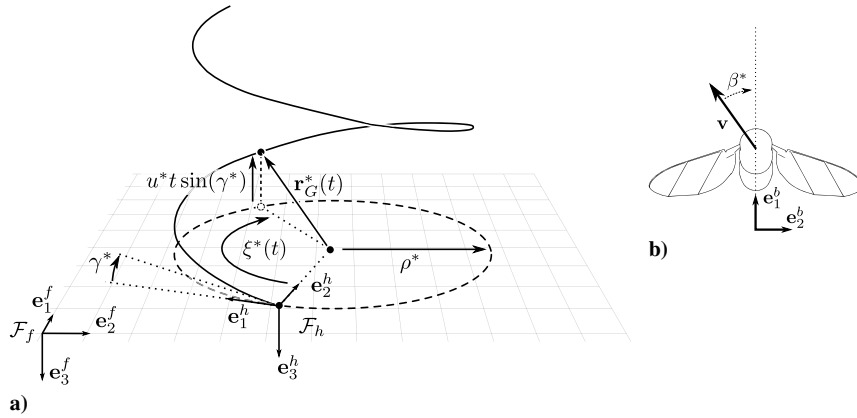


Fig. 5 Representations of a) geometry of the robot trajectory in a coordinated turn and b) visualization of the sideslip angle.

$$\rho = \frac{V}{\dot{\xi}} \quad (39)$$

From the coordinated turn definition, the special cases of longitudinal, lateral, and hovering flight can be obtained by virtue of the same command input [Eq. (38)], as explained in the remainder of this section.

The output equation [Eq. (3)] can be obtained by establishing a functional relationship between the full command input \mathbf{y} , defined in Eq. (38), and the robot state \mathbf{x} defined in Eq. (16). Letting $\mathbf{v} = [u \ v \ w]^T$ denote the body-frame robot velocity, the robot airspeed is given by

$$V = \|\mathbf{v}\| = \sqrt{(u^2 + v^2 + w^2)} \quad (40)$$

and the climb angle is

$$\gamma = \arctan\left[\frac{\dot{z}}{\sqrt{(\dot{x}^2 + \dot{y}^2)}}\right] \quad (41)$$

The turn rate is equal to the time rate of change of the yaw angle

$$\dot{\xi} = \dot{\phi} \quad (42)$$

and the sideslip angle is given by

$$\beta = \arctan\left(\frac{-v}{u}\right) \quad (43)$$

completing the definition of the nonlinear vector function in the output equation [Eq. (3)].

When computing the set points for fixed-wing aircraft, the desired command input \mathbf{y}^* directly specifies a subset of the state variables in \mathbf{x}^* , whereas the remaining state values are computed so as not to oppose the steady maneuver commanded by \mathbf{y}^* . When a flapping-wing robot performs a coordinated turn, the robot linear and angular velocities, \mathbf{v} and $\boldsymbol{\omega}_b$, are constrained to rotate about \mathbf{e}_3^f at the desired turn rate $\dot{\xi}^*$. This rotation is computed using the rotation matrix $\mathbf{R}^* \triangleq \mathbf{R}(\mathbf{e}_3^f, T\dot{\xi}^*)$, according to the convention in Appendix C. Without loss of generality, let $t_0 = 0$ denote the initial time at which the maneuver is initiated by a command input value \mathbf{y}^* provided by an operator or guidance algorithm. Constraints on the body Euler angles and the body position vector follow from the constraints on body angular rate and velocity, and they are written using an intermediate frame \mathcal{F}_h that coincides with the inertial frame \mathcal{F}_f rotated about \mathbf{e}_3^b by the robot-body yaw angle at the onset of the maneuver, i.e., $\phi(0)$. Then, at the end of a flapping period T , the desired state for a coordinated turn command \mathbf{y}^* is given by

$$\mathbf{x}^*(T) = \begin{bmatrix} [\mathbf{x}_w(0)]^T & [\mathbf{r}_G^*(T)]^T & [\boldsymbol{\Theta}^*(T)]^T & [\mathbf{R}^* \mathbf{v}(0)]^T & [\mathbf{R}^* \boldsymbol{\omega}_b(0)]^T \end{bmatrix}^T \quad (44)$$

where the desired orientation is

$$\boldsymbol{\Theta}^*(T) = \boldsymbol{\Theta}(0) + [T\dot{\xi}^* \ 0 \ 0]^T \quad (45)$$

the desired position is

$$\mathbf{r}_G^*(T) = \mathbf{r}_G(0) - V^* T \sin(\gamma^*) \mathbf{e}_3^f + \rho^* \cos(\gamma^*) (\mathbf{e}_2^h - \mathbf{R}^* \mathbf{e}_2^h) \quad (46)$$

and $\mathbf{e}_2^h = \mathbf{R}[\mathbf{e}_3^f, \phi(0)]\mathbf{e}_2^f$.

B. Longitudinal Flapping Flight

Longitudinal flight consists of robot motions that are confined to its sagittal plane, namely, the plane normal to \mathbf{e}_2^b through G . Therefore, longitudinal flight is a special case of the coordinated turn in which both the turn rate and sideslip angle are zero. The airspeed is nonnegative and the climb angle can be either positive (ascent) or negative (descent), such that longitudinal command inputs are in the form

$$V^* > 0, \quad \gamma^* \leq 0, \quad \dot{\xi}^* = 0, \quad \beta^* = 0 \quad (47)$$

and the flapping robot is said to be flying steady level when $\gamma^* = 0$. The desired center-of-gravity position in Eq. (46) is formulated in terms of the turn radius which goes to infinity for longitudinal maneuvers. Therefore, the longitudinal set point is obtained by decomposing \mathbf{r}_G^* into its \mathbf{e}_1^h and \mathbf{e}_2^h components:

$$\mathbf{r}_G^*(T) = \mathbf{r}_G(0) - V^* T \sin(\gamma^*) \mathbf{e}_3^f + \rho^* \cos(\gamma^*) [\mathbf{e}_2^h - \mathbf{e}_2^h \cos(\dot{\xi}^* T) + \mathbf{e}_1^h \sin(\dot{\xi}^* T)] \quad (48)$$

Then, \mathbf{r}_G^* can be reformulated solely in terms of the desired airspeed V^* as follows. The vector $\mathbf{r}_G(0)$ is subtracted from both sides of Eq. (48), and the equation

$$[\mathbf{r}_G^*(T) - \mathbf{r}_G(0)] \cdot \mathbf{e}_1^h = \rho^* \cos(\gamma^*) \sin(\dot{\xi}^* T) \quad (49)$$

is obtained by taking the inner product with \mathbf{e}_1^h . Then, since $\dot{\xi} = 0$, the desired position can be simplified to

$$[\mathbf{r}_G^*(T) - \mathbf{r}_G(0)] \cdot \mathbf{e}_1^h = V^* T \cos(\gamma^*) \quad (50)$$

which defines the difference in position after a single flapping period based on the commanded speed V^* and the length of time T traveling at that speed. From Eqs. (48) and (50), it can be easily shown that the following holds:

$$\mathbf{r}_G^*(T) = \mathbf{r}_G(0) - V^*T \sin(\gamma^*)\mathbf{e}_3^f + V^*T \cos(\gamma^*)\mathbf{e}_1^h \quad (51)$$

Then, the set-point state of a longitudinal quasi-steady maneuver specified by the command input in Eq. (47) is given by

$$\mathbf{x}^*(T) = \begin{bmatrix} \mathbf{x}_w^T(0) & [\mathbf{r}_G^*(T)]^T & \Theta^T(0) & \mathbf{v}^T(0) & \omega_b^T(0) \end{bmatrix}^T \quad (52)$$

C. Lateral Flapping Flight

Lateral flight consists of robot motions that are confined to its coronal plane, namely, the plane normal to \mathbf{e}_1^h through G . For the RoboBee, lateral flight can be achieved by setting the sideslip angle equal to $\pi/2$, thereby restricting the dominant flight motions to the coronal plane. Then, lateral command inputs take the form

$$V^* > 0, \quad \gamma^* \leq 0, \quad \dot{\xi}^* = 0, \quad \beta^* = \frac{\pi}{2} \quad (53)$$

and allow the robot to maintain a sideslip angle as shown in Fig. 5b, which may be useful, for example, for maintaining sensory orientation with respect to a moving target. Then, the desired state can be obtained from \mathbf{y}^* as shown in Eq. (52), only now the velocity vector \mathbf{v} points in the \mathbf{e}_2^h direction; therefore, the center-of-gravity position is given by

$$\mathbf{r}_G^*(T) = \mathbf{r}_G(0) - V^*T \sin(\gamma^*)\mathbf{e}_3^f + V^*T \cos(\gamma^*)\mathbf{e}_2^h \quad (54)$$

D. Hovering Flapping Flight

Flapping hovering flight can be viewed as a special case of longitudinal flight in which the robot has zero airspeed and zero climb angle. Therefore, hovering command inputs take the form

$$\mathbf{y}^* = \mathbf{0} \quad (55)$$

In this case, it is assumed that at the initial time $t_0 = 0$, the robot is already at the desired altitude and orientation and must remain there by hovering. If changes in any of the robot position and orientation variables are desired, then they must be achieved by means of one of the aforementioned maneuvers. In other words, when hovering, the robot state after one flapping period T must remain equal to the initial condition:

$$\mathbf{x}^*(T) = \mathbf{x}(0) \quad (56)$$

At any given time, the desired command input \mathbf{y}^* is provided by an operator or guidance algorithm so as to specify a desired maneuver, and it is held constant until the next step change in \mathbf{y}^* to allow the robot to reach steady state. The robot dynamic stability and dominant modes of motion analyzed in Sec. VII show that the aforementioned maneuvers (Secs. V.A–V.D) are stable; thus, steady state can be achieved for the desired state value \mathbf{x}^* . The mixing logic that determines the trim control settings \mathbf{u}^* is obtained by integrating the dynamic equation [Eq. (1)] numerically, i.e.,

$$\mathbf{x}(T) = \int_0^T \mathbf{f}[\mathbf{x}(\tau), \mathbf{u}(\tau), \mathbf{p}, \tau] + \mathbf{x}(0) \quad (57)$$

subject to the terminal constraint

$$\mathbf{x}(T) = \mathbf{x}^*(T) \quad (58)$$

where $\mathbf{x}^*(T)$ is the desired state specified by the command input obtained from Eq. (44), Eq. (52), or Eq. (56). In this paper, the numerical integration in Eq. (57) is performed using the separated Hermite–Simpson rule [82] (Ref. [83] chap. 4). Then, the constant trim control vector that simultaneously satisfies Eqs. (57) and (58) completes the definition of the desired set point $(\mathbf{x}^*, \mathbf{u}^*) \in U$. When no solution exists, the desired maneuver falls outside of the flight envelope, and therefore cannot meet the physical limitations of the

FWMAV. The full trim map U , defined in Eq. (4), is obtained by discretizing the range of possible values of every command input variable in Eq. (38) and by computing the corresponding set points, including them in the set U whenever a solution is found.

Because the robot dynamics are nonlinear, it is both possible and common for set points to exist but be unstable. In this case, any small perturbations from the set point will cause the robot trajectories to move away from the unstable equilibrium. The dominant mode analysis in Sec. VII provides a foundation for understanding stable and unstable flight conditions and, eventually, how unstable conditions may be stabilized by a feedback controller [14,83].

VI. FWMAV Flight Envelopes

The propulsion, design, and physical parameters of the robot impose physical limitations on the achievable operating conditions, as well as the set points for which commanded maneuvers are possible. The boundary of the trim map ∂U provides the minimum and maximum values of trim control settings from which the flight envelope may be obtained. In designing autonomous controllers for flapping-wing robots, the flight envelope defines the range of conditions within which a forward flight controller is capable of maintaining the robot at a desired set point. Once a robot is built and operational, the flight envelope is used to determine the operating conditions at which the robot can safely operate without damaging the actuators. Also, by analyzing the sensitivity of the flight envelope boundaries to the physical parameters of a robot, the flight envelope can be used to help design new robots and ensure that they meet minimum performance requirements.

Because propulsion is provided entirely by flapping wings, one of the key physical limitations in FWMAV flight consists of the wing-motion range imposed by the wing joint. In the case of the RoboBee, for example, the joint limits determine the maximum allowable values of wing stroke angle. Thus, the flight envelope is obtained by evaluating the wing trajectories required to achieve a desired set point. For a given set point $(\mathbf{x}^*, \mathbf{u}^*)$, the maximum stroke angle required for each wing i , denoted by $\max(|\phi_i|)$, is obtained by integrating the equations of motion [Eq. (59)]. The maximum stroke angle required for longitudinal and lateral flight is plotted as a function of the commanded airspeed V^* and climb angle γ^* in Fig. 6. The radial distance from the center of the plot indicates the values of commanded speed V^* in meters per second, and the angular coordinate indicates the values of commanded climb angle γ^* in degrees. In the case of the RoboBee, from the fabrication steps, the maximum allowable stroke angle is found equal to 55 deg, leading to the envelopes plotted by the black solid lines in Fig. 6.

The longitudinal flight envelope in Fig. 6a shows that the joint limits, imposed by the robot fabrication, constrain the maximum ascending flight speed to approximately 1.5 m/s. It can also be seen that, in descending flight, higher speeds can be achieved and the wing joint design imposes no limitations. From the lateral flight envelope in Fig. 6b, it can be seen that the maximum stroke angle mainly limits the maximum vertical flight speed and that it is only a weak function of the climb angle because the black solid line in Fig. 6b remains almost horizontal. This is noticeably different from the longitudinal case, in which the nonzero climb angle required to maintain forward flight varies significantly with the climb angle, as illustrated by the black solid line in Fig. 6a curving sharply downward toward the edges of the envelope.

VII. FWMAV Stability and Dominant Modes of Motion

All of the flapping-robot maneuvers described in Sec. V, with the exception of hovering flight, consist of quasi-steady equilibria. This is because the body-frame velocities, angular rates, and wing state variables in \mathbf{x}_1 are T periodic, whereas the state variables in \mathbf{x}_2 change over time, for example, because they are integrals of \mathbf{x}_1 . This section shows that dynamic mode decomposition can be used to identify stable and unstable dominant modes of motion that are locally linear and can be identified in both numerical and physical full-envelope experiments on the RoboBee. Due to the periodic nature

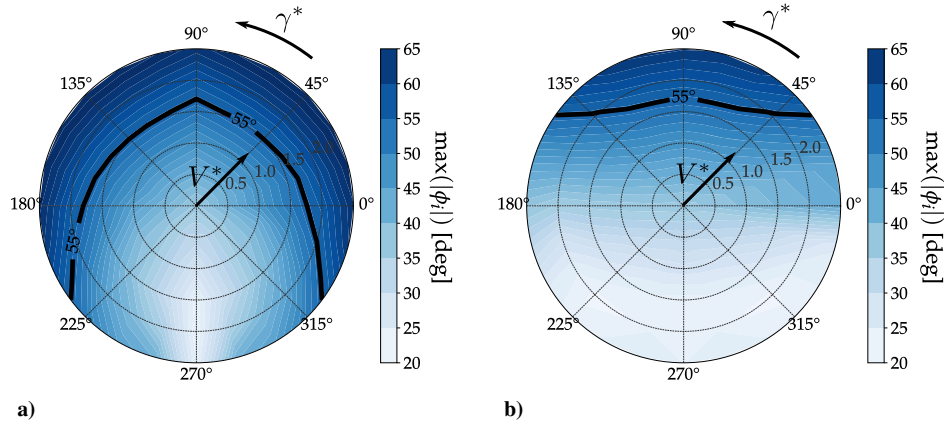


Fig. 6 Robot a) longitudinal and b) lateral flight envelopes provide boundaries on allowable airspeed V^* in meters per second and climb angle γ^* in degrees as a function of maximum stroke angle (color bar), which for the RoboBee is found to be $\max(|\phi_i|) = 55$ deg (black solid line).

of flapping-wing flight stability is first analyzed numerically by discretizing the dynamic equation [Eq. (1)] with respect to time, and, then, by linearizing the dynamics about the dominant modes of motion that can be described as attractors in the robot eigenplanes (Sec. VIII).

Let the discrete-time step be denoted by $t_k = kT$, $k = 0, 1, 2, \dots$, and the discrete-time state and control vectors be denoted by $\mathbf{x}_k = \mathbf{x}(t_k)$ and $\mathbf{u}_k = \mathbf{u}(t_k)$, respectively. Then, the FWMAV dynamics in discrete time can be approximated by the difference equation:

$$\mathbf{x}_{k+1} = \mathbf{f}_D(\mathbf{x}_k, \mathbf{u}_k, \mathbf{p}) + \mathbf{x}_k, \quad \mathbf{x}(t_0) = \mathbf{x}_0 \quad (59)$$

where

$$\mathbf{f}_D(\mathbf{x}_k, \mathbf{u}_k, \mathbf{p}) \triangleq \int_{t_k}^{t_{k+1}} \mathbf{f}[\mathbf{x}(t), \mathbf{u}(t), \mathbf{p}, t] dt \quad (60)$$

For an actuated system, an equilibrium condition consists of a set point $(\mathbf{x}^*, \mathbf{u}^*)$ at which all of the state time derivatives vanish; thus,

$$\mathbf{f}_D(\mathbf{x}^*, \mathbf{u}^*, \mathbf{p}) = \mathbf{0} \quad (61)$$

At a quasi-steady equilibrium, all time derivatives of \mathbf{x}_1 vanish but \mathbf{x}_2 varies in time, for example, because it contains integrals of \mathbf{x}_1 . For both steady and quasi-steady equilibrium conditions, the FWMAV set point $(\mathbf{x}^*, \mathbf{u}^*)$ can be computed as shown in Sec. V.

Then, the robot linear modes of motion and their stability are analyzed by linearizing the difference equation [Eq. (59)] about the set point

$$\mathbf{x}_{k+1} = \nabla \mathbf{f}_D|_{(\mathbf{x}^*, \mathbf{u}^*)} \mathbf{x}_k \quad (62)$$

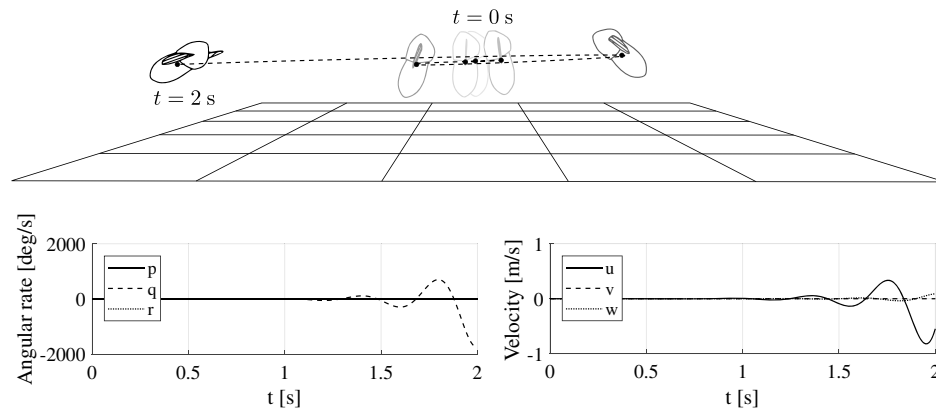


Fig. 7 Unstable longitudinal mode in hovering flight illustrated by a robot trajectory (top) and time histories of body-frame pitch rate (left) and forward velocity (right).

where $\nabla \mathbf{f}_D|_{(\mathbf{x}^*, \mathbf{u}^*)}$ is the Jacobian matrix evaluated at the set point. Eigendecomposition is used to express the solution of Eq. (62) in terms of the eigenvalues $\lambda_i = \sigma_i \pm i\omega_i$ and eigenvectors $\mathbf{v}_i = \mathbf{u}_i \pm i\mathbf{w}_i$ of the Jacobian as follows:

$$\mathbf{x}_k = \sum_{i=1}^n \kappa_i \lambda_i^k \mathbf{v}_i \quad (63)$$

where $\kappa_i \in \mathbb{R}$ are coefficients that depend on the initial conditions \mathbf{x}_0 , and the index i labels the dominant mode.

Throughout the flight envelope two dominant linear modes were identified both in experiments and simulations: 1) a quasi-oscillatory motion dominated by pitching and forward motions called the *longitudinal mode*; and 2) a quasi-oscillatory motion dominated by lateral motion and body roll oscillations called the *lateral mode*, coupled with yawing and pitching motions in forward flight.

The aforementioned modes were found to be stable or unstable depending on the flight regime. All other modes were found to dampen out relatively quickly and to be stable throughout the flight envelope. Thus, the rest of the discussion focuses on the longitudinal and lateral modes defined earlier in this paper. Figures 7 and 8 illustrate the unstable motions associated with these modes at the hovering equilibrium point. The trajectories plotted in these figures are solutions to Eq. (62), given initial conditions that lie in the spaces of the longitudinal and lateral eigenvectors, \mathbf{v}_o and \mathbf{v}_a , where the subscripts o and a denote the longitudinal and lateral modes, respectively. As shown in Fig. 7, the longitudinal mode is primarily characterized by oscillations in pitch rate q and forward velocity u . The lateral mode near hovering, instead, is characterized primarily by oscillations in roll rate p and lateral velocity v , as shown in Fig. 8. As forward flight speed increases, the lateral mode also couples with pitch rate q and yaw rate r .

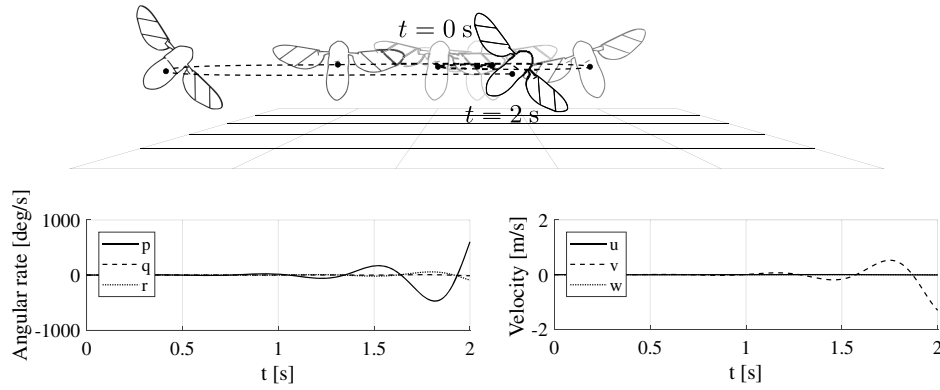


Fig. 8 Unstable lateral mode in hovering flight illustrated by a robot trajectory (top) and time-histories of body-frame roll rate (left) and lateral velocity (right).

To visualize changes in the eigenvalues for the longitudinal mode throughout the flight envelope, the longitudinal damping ratio $\zeta_o = -\cos[\angle \ln(\lambda_o)]$ [where \angle denotes the angle in the complex plane, e.g., $\angle \lambda_i = \text{atan}(\omega_i/\sigma_i)$] is plotted for longitudinal flight as a function of commanded airspeed V^* and climb angle γ^* in Fig. 9a (with $\xi^* = \beta^* = 0$) and for a level coordinated turn as a function of V^* and turn rate ξ^* in Fig. 9b (with $\gamma^* = \beta^* = 0$). Near hovering flight and in most regimes of low-speed flight and climbing flight, the longitudinal mode is unstable, having two complex conjugate eigenvalues each with a magnitude greater than unity. As indicated by the red region in Fig. 9a, the longitudinal mode becomes a stable, underdamped mode at moderate flight speeds when $\gamma^* \leq 0$. A third regime exists for nearly vertical high-speed flight, outlined in

the upper-right-hand corner of Fig. 9a approximately where $\gamma^* > 60$ deg and $V^* > 1.3$ m/s. In this regime, the longitudinal mode is characterized by an unstable exponentially divergent motion and has two distinct purely real eigenvalues. For level turning flight, the longitudinal mode is unstable except for low turn rates at high speed ($\xi^* < 120$ deg/s and $V^* > 1$ m/s), where it is characterized by underdamped stable oscillations, plotted by the red area in Fig. 9b. The transition from unstable to stable flight occurs at higher flight speeds as ξ^* increases.

The lateral mode eigenvalues are visualized throughout the flight envelope by plotting the lateral damping ratio, $\zeta_a = -\cos[\angle \ln(\lambda_a)]$, as a function of commanded airspeed and climb angle, as shown in Fig. 10. The lateral mode in the longitudinal flight regime can be

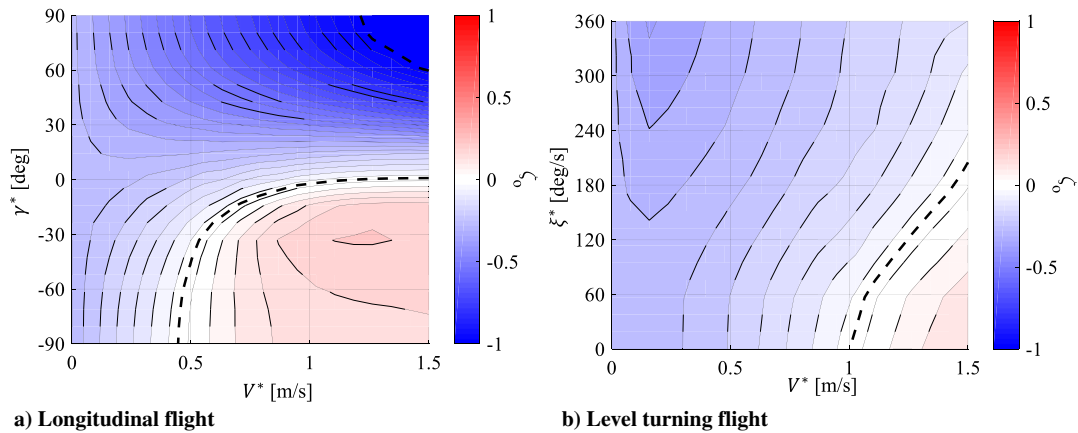


Fig. 9 Longitudinal damping ratio for level turning flight, where the unstable regions are plotted in blue and the stable regions are plotted in red.

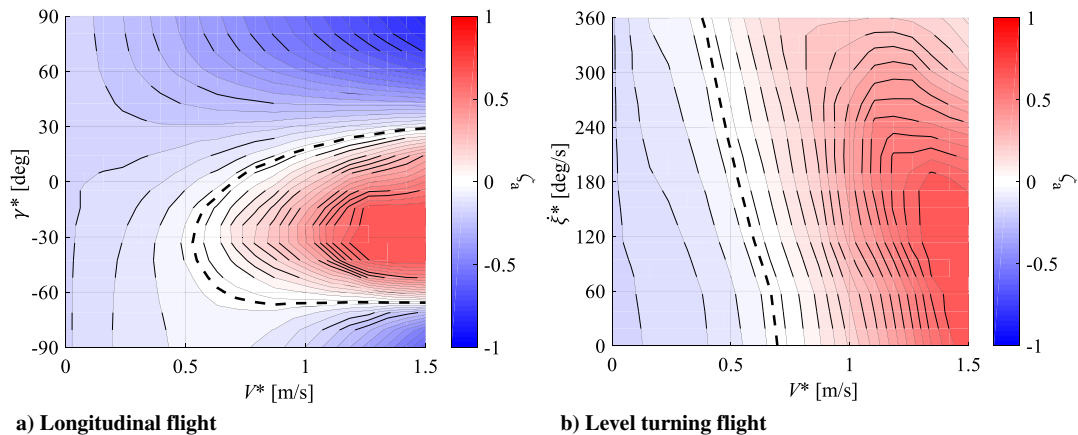


Fig. 10 Lateral damping ratio for longitudinal flight and level turning flight, where the unstable regions are plotted in blue and the stable regions are plotted in red.

divided into stable and unstable regions, as shown in Fig. 10a. The unstable region occupies the majority of the flight envelope and is characterized by two complex conjugate eigenvalues with magnitude greater than one. Above moderate forward flight speeds, the lateral mode is characterized by stable underdamped solutions, plotted by the red region in Fig. 10a. In the level turning flight regime, the transition from unstable to stable lateral flight occurs at lower flight speeds as $\dot{\xi}^*$ increases, as shown in Fig. 10b.

An important special case of longitudinal flight is level forward flight, where $V^* > 0$ and $\gamma^* = 0$. In level forward flight, the lateral

mode is stable above flight speeds of $V^* \approx 0.7$ m/s, and the longitudinal mode is stable above flight speeds of $V^* \approx 1.0$ m/s. At forward flight speeds greater than 1.0 m/s, all linear modes of forward level flight are stable. The regions of stability for all regimes of longitudinal flight and level turning flight are found by taking the union of the stable regions for both the longitudinal and lateral modes from Figs. 9 and 10. The result of this union is plotted in Fig. 11.

In stable flight regimes, the longitudinal and lateral modes exhibit different motions compared with their motions near hovering (Figs. 7 and 8). Figures 12 and 13 illustrate the stable motions associated with

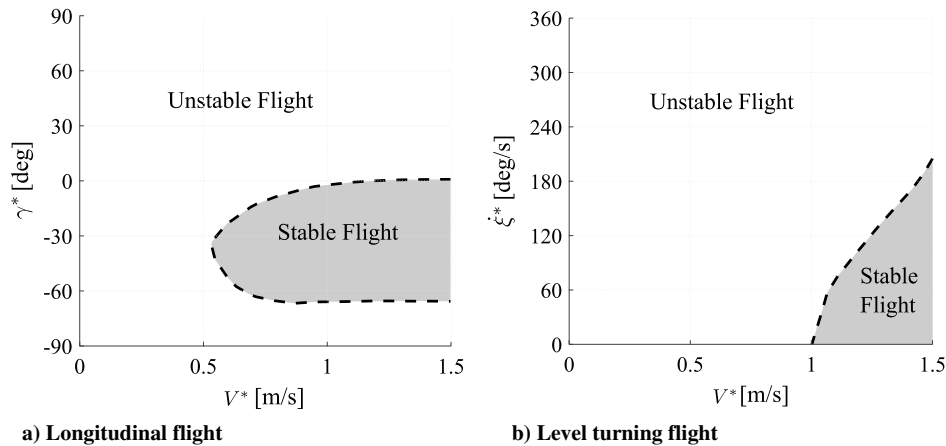


Fig. 11 Regions of stable and unstable a) longitudinal and b) level turning flight obtained from the transition boundaries in Figs. 9 and 10.

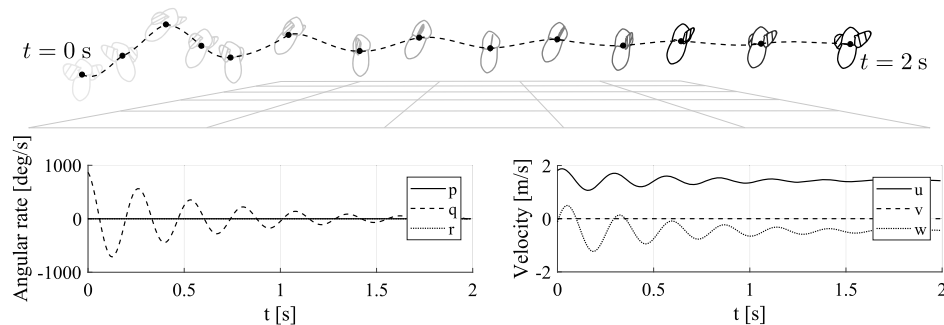


Fig. 12 Longitudinal mode in forward level flight at 1.5 m/s illustrated by a robot trajectory (top) and time histories of body-frame components of angular (left) and linear (right) velocities.

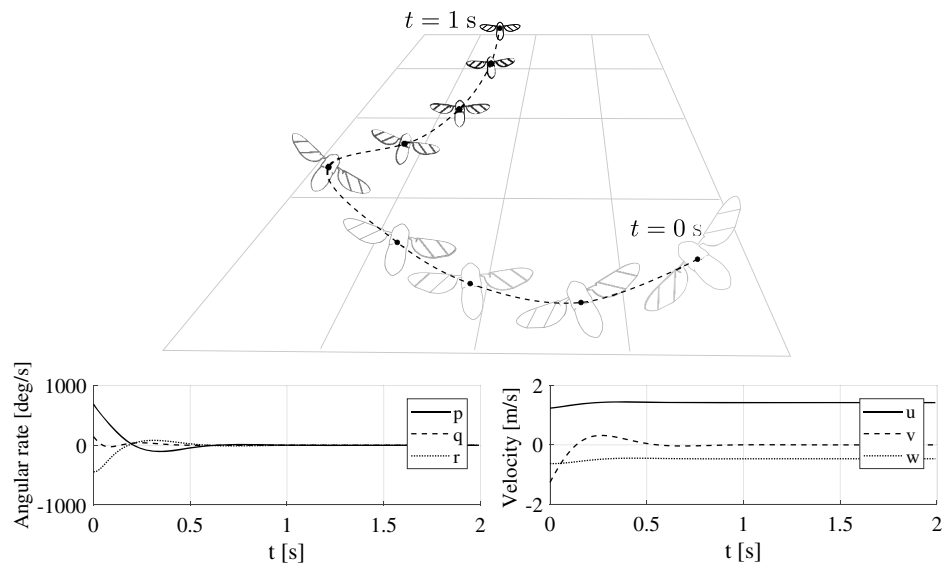


Fig. 13 Lateral mode in forward level flight at 1.5 m/s illustrated by a robot trajectory (top) and time histories of body-frame components of angular (left) and linear (right) velocities.

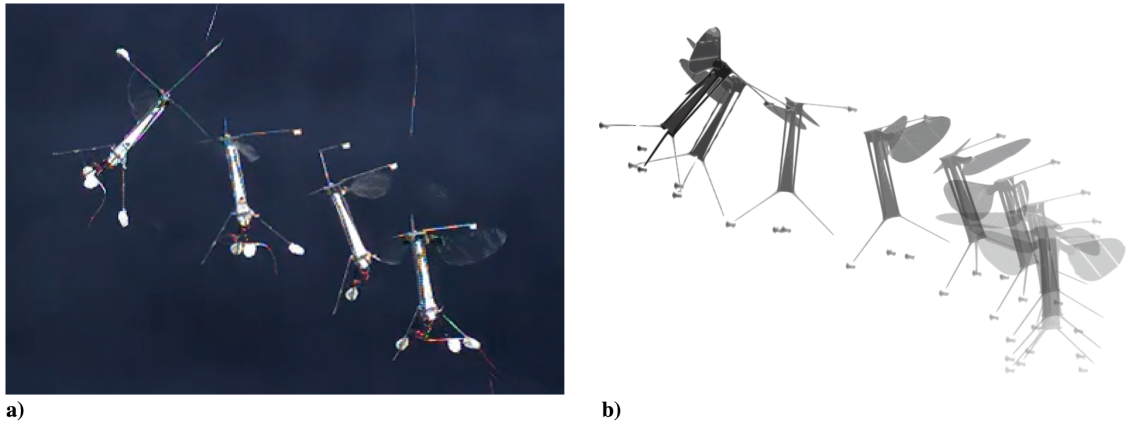


Fig. 14 Comparison of open-loop longitudinal unstable flight in a) the physical robot and b) the model showing qualitatively similar behaviors.

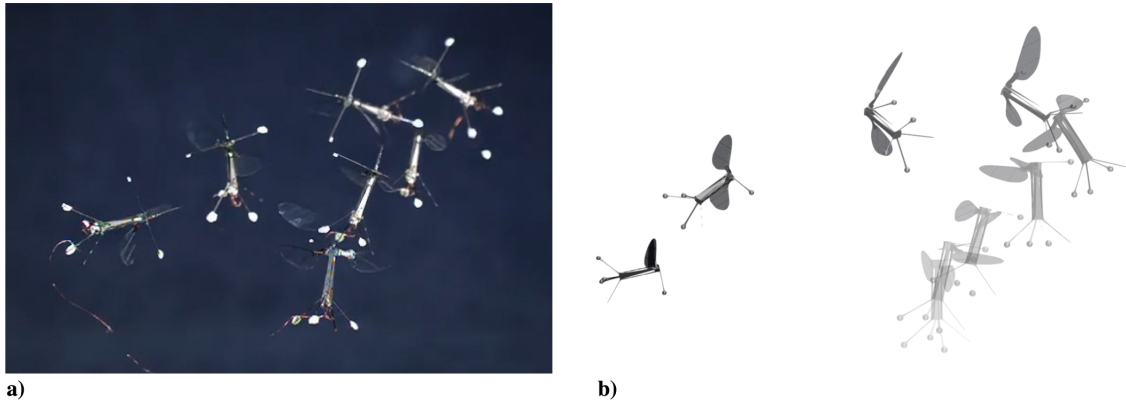


Fig. 15 A second comparison of open-loop asymmetrical unstable flight in a) the physical robot and b) the model, also showing qualitatively similar behaviors.^{††}

the longitudinal and lateral modes for forward level flight with $V^* = 1.5$ m/s. Compared with the mode shape at hovering, the longitudinal mode in forward flight couples more strongly with the e_3^b component of body velocity w such that the magnitude of oscillations in w is roughly twice the magnitude of the oscillations in u . Near $V^* = 1.5$ m/s, the longitudinal mode is very lightly damped, thus requiring on the order of hundreds of wing beats to dampen out all oscillations and reach steady state. In forward flight, the lateral mode resembles the Dutch roll mode characteristic of fixed-wing aircraft [27]. In fact, the robot exhibits coupled rolling and yawing motions that result in passively stable banked turns. The oscillations in p and r are approximately 180 deg out of phase, whereas the same oscillations are nearly in phase with one another near hovering flight (Fig. 8). Also, in forward flight the lateral mode is more highly damped than the longitudinal mode and settles to steady state in under 100 wing beats.

VIII. Experimental Results and Validation

Validating FWMAV models against experimental data is complicated due to the nonlinear and unstable nature of flapping-wing flight, even in the vicinity of hovering and other stable maneuvers. In this section, the RoboBee dynamic model described in Sec. III is validated by examining both dominant linear modes and nonlinear unstable behaviors obtained in simulations and experiments conducted at the Harvard Microrobotics Laboratory. As a first step, several open-loop flight trials were conducted on the RoboBee near hovering, starting at a zero body velocity and an upright vertical position. Then, a constant control input was applied to the robot using the set point corresponding to the desired hovering flight condition.

^{††}Video available at <https://youtu.be/qj-VbJiVVk4> [retrieved 29 Sept. 2020].

Fifteen tests were conducted in this manner and the sequences of images recorded from two representative experimental trials are shown in Figs. 14a and 15a. Using the same initial conditions and parameters as those used in these experiments, the sequences of images rendered from the RoboBee dynamic model, plotted in Figs 14b and 15b, show that the model adequately captures nonlinear behaviors observed in the RoboBee. Although it is challenging to recreate the set of initial conditions and disturbances of every experimental trial, overall the dynamic model was found to exhibit most of the same qualitative open-loop behaviors as the physical robot.

Following the dynamic model validation, data-driven dynamic mode decomposition [68,69] was used to extract the longitudinal and lateral dominant modes of motion from the RoboBee numerical-simulation and experimental data obtained via the Vicon system. Assuming the dynamics are approximately linear near hovering, the state observed at one time step depends on the state observed at the previous time step, according to the linear relationship

$$\mathbf{X}_2 = \mathbf{A}\mathbf{X}_1 \quad (64)$$

where \mathbf{A} is a state-space matrix learned from data and, for $N = 15$ experiments,

$$\mathbf{X}_1 \triangleq [\mathbf{x}_1 \ \mathbf{x}_2 \ \dots \ \mathbf{x}_{N-1}] \quad \text{and} \quad \mathbf{X}_2 \triangleq [\mathbf{x}_2 \ \mathbf{x}_3 \ \dots \ \mathbf{x}_N] \quad (65)$$

The experimental eigenvalues and eigenvectors of \mathbf{A} correspond to the linear modes of the physical robot near hovering flight, to be compared to the linear modes of the model obtained from the Jacobian matrix $\nabla f_D|_{(x^*, u^*)}$, evaluated at the hovering set point. The matrix \mathbf{A} is learned from data using Singular Value Decomposition (SVD):

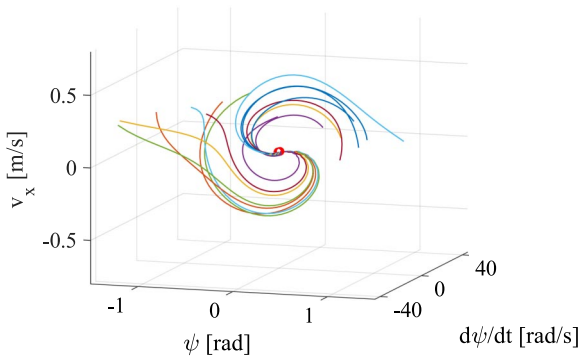
$$A = X_2 V \Sigma^{-1} U^H \quad (66)$$

where $(\cdot)^H$ denotes the Hermitian transpose, $U \in \mathbb{C}^{n \times r}$, $\Sigma \in \mathbb{C}^{r \times r}$, $V \in \mathbb{C}^{N \times r}$, and $r \leq n$ is the rank of the SVD approximation of X_1 . Measurement noise can be suppressed by restricting the rank r so that the decomposition includes only the dominant singular modes. The eigenvectors of A are found to correspond to the longitudinal and lateral modes identified in the RoboBee dynamic model. Furthermore, when the trajectories obtained from the experimental data are plotted in the phase plane, they can be seen to live in the longitudinal and lateral subspaces and to match the phase portraits obtained from the dynamic model, as shown in Fig. 16. These qualitative results are further validated by quantitative comparisons of the robot eigenvectors and eigenplanes, as follows.

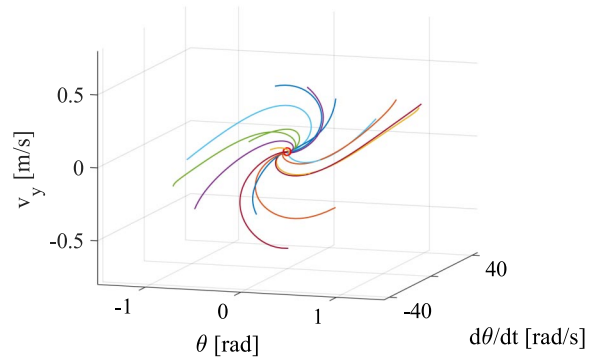
The longitudinal mode comprises predominantly terms corresponding to the state variables ψ , v_x , and $d\psi/dt$. Let $v_o \in \mathbb{R}^3$ and $\tilde{v}_o \in \mathbb{R}^3$ denote the longitudinal mode eigenvectors obtained from the RoboBee model and the experimental data, respectively. Then, the unit normals of the model and experimental eigenplanes are given by

$$n_o = \text{Re}(v_o) \times \text{Im}(v_o), \quad \text{and} \quad \tilde{n}_o = \text{Re}(\tilde{v}_o) \times \text{Im}(\tilde{v}_o) \quad (67)$$

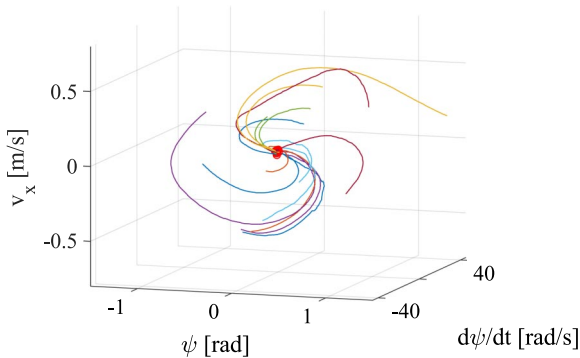
respectively, where $\text{Re}(\cdot)$ and $\text{Im}(\cdot)$ denote the real and imaginary parts of the vector. As shown in Fig. 17a, the experimental trajectories in the longitudinal mode lie near the eigenplane normal to \tilde{n}_o . This occurs because the longitudinal mode dominates the evolution of ψ , v_x , and $d\psi/dt$ near hovering; thus, the state trajectories remain near



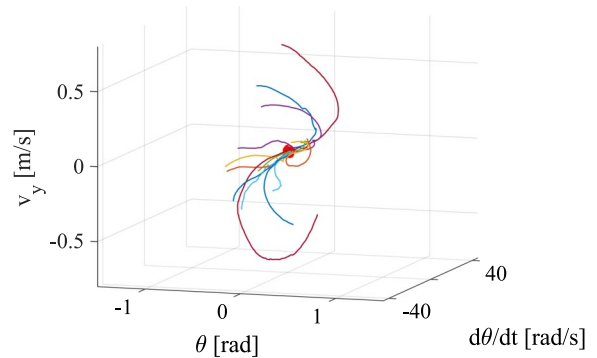
a) Simulated trajectories in the longitudinal subspace



b) Simulated trajectories in the lateral subspace

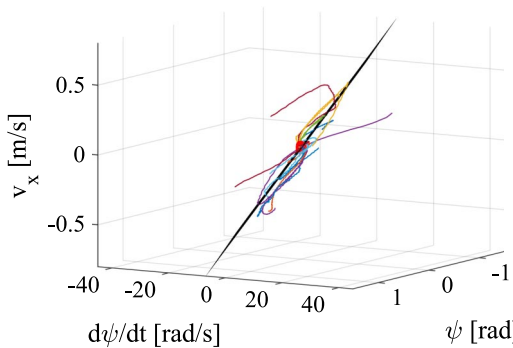


c) Experimental trajectories in the longitudinal subspace

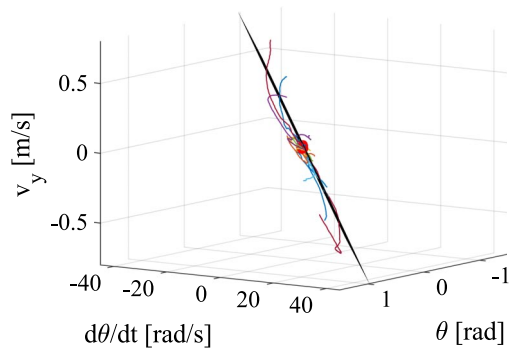


d) Experimental trajectories in the lateral subspace

Fig. 16 The phase portraits obtained using the RoboBee model are qualitatively very similar to those obtained experimentally for a,c) longitudinal and b, d) lateral modes.



a) Eigenplane corresponding to longitudinal flight mode



b) Eigenplane corresponding to lateral flight mode

Fig. 17 Experimental phase portraits obtained near open-loop hovering conditions show trajectories lie near dominant eigenplanes (black lines) corresponding to a) longitudinal and b) lateral modes.

Table 1 Natural frequency and damping ratio of dominant modes obtained numerically and experimentally

Mode	ω_n , rad/s	ζ
Longitudinal (experiment)	22.8	-0.35
Longitudinal (simulation)	19.0	-0.17
Lateral (experiment)	11.1	-0.67
Lateral (simulation)	14.3	-0.61

the space spanned by the real and imaginary parts of the longitudinal mode eigenvector.

Similarly, the lateral mode contains dominant terms corresponding to the state variables θ , v_y , and $d\theta/dt$, implying that the trajectories of these variables must remain near the space spanned by the real and imaginary parts of the lateral mode eigenvector. Let $\mathbf{v}_a \in \mathbb{R}^3$ and $\tilde{\mathbf{v}}_a \in \mathbb{R}^3$ denote the lateral mode eigenvectors obtained from the RoboBee model and experimental data, respectively. Then, the unit normals of the model and experimental eigenplanes are given by

$$\mathbf{n}_a = \text{Re}(\mathbf{v}_a) \times \text{Im}(\mathbf{v}_a), \quad \text{and} \quad \tilde{\mathbf{n}}_a = \text{Re}(\tilde{\mathbf{v}}_a) \times \text{Im}(\tilde{\mathbf{v}}_a) \quad (68)$$

respectively. As shown in Fig. 17b, the experimental trajectories in the lateral mode lie near the eigenplane normal to $\tilde{\mathbf{n}}_a$. Therefore, for both dominant modes, the experimental trajectories lie very near the eigenplanes identified via DMD.

The eigenplane unit normals obtained from experimental data ($\tilde{\mathbf{n}}_o$ and $\tilde{\mathbf{n}}_a$) are compared to those obtained from the model (\mathbf{n}_o and \mathbf{n}_a) by taking the dot products

$$\mathbf{n}_o^T \tilde{\mathbf{n}}_o = 0.98, \quad \mathbf{n}_a^T \tilde{\mathbf{n}}_a = 0.99 \quad (69)$$

Because the preceding dot products are close to one, it follows that the experimental eigenplanes are close to parallel to the model eigenplanes. Additionally, the dominant mode natural frequency of $\omega_i = |\ell_n(\lambda_i)/T|$ and the damping ratio of $\zeta_i = -\cos(\angle \ell_n(\lambda_i))$, obtained from the model are compared to those obtained experimentally. As shown by the results in Table 1, both parameters are matched satisfactorily by the RoboBee model in both longitudinal and lateral modes.

As discussed in Sec. VII, an important characteristic of asymmetric flapping-wing flight is the coupling between roll and yaw motions in lateral flight mode. To validate this characteristic, the RoboBee was clamped vertically and its wings were commanded to flap at a constant amplitude corresponding to hovering flight, while a high-speed camera mounted above the robot captured wing stroke and pitch angles. To measure the effects of forward flight on wing pitch angles, 10 baseline trials were conducted with a headwind of $v = 0.5$ m/s along the \mathbf{e}_1^b axis ($\beta = 0$ deg). Ten more trials were conducted at the same wind speed and a sideslip angle of $\beta = 30$ deg. Figure 18 shows several still frames from the baseline, with the wing from the nonzero-sideslip study overlaid in red. These images show that the right- and left-wing pitch angles are affected asymmetrically

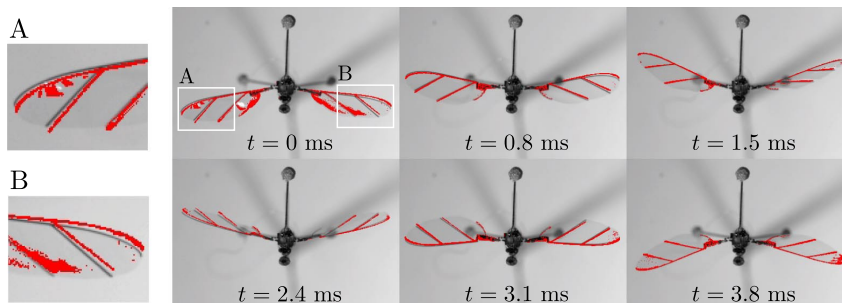


Fig. 18 Comparison between the wing trajectories obtained at a 0 deg sideslip angle (shown in grayscale) and at a 30 deg sideslip angle (shown in red), for a constant 0.5 m/s headwind.

when the sideslip angle between the \mathbf{e}_1^b axis and the wind direction is nonzero.

The projected angle between the first wing spar and the leading edge is used to compute the wing pitch angle from the high-speed video using the known geometry of the wing. The box and whisker plots in Fig. 19 show that the mean pitch angles of the right and left wings, denoted by $\bar{\psi}_r$ and $\bar{\psi}_l$, differ from the zero-sideslip baseline when the sideslip angle is increased to 30 deg (mean values across trials shown by red bar). In fact, as the wind direction shifts to one (left) side of the robot and the sideslip angle increases, the magnitude of the corresponding (left) wing's mean pitch angle decreases to zero, whereas the other (right) wing's mean pitch angle remains largely unchanged. For a constant wind speed, the dynamic model predicts that the magnitudes of the mean pitch angles of both wings are largest when there is a direct headwind, i.e. $\beta = 0$ deg. As the sideslip angle increases, the magnitudes of the mean pitch angles decrease asymmetrically, as demonstrated by the experimental results plotted in Fig. 19.

To further explore the roll-yaw couplings in lateral mode, the RoboBee model is used to study the mean pitch angles of the right and left wing as a function of increasing wind speed while holding the sideslip angle constant at $\beta = 30$ deg. The results in Fig. 20 show that the mean wing pitch angle directly affects the stroke-averaged aerodynamic forces acting on each wing and, in turn, the stroke-averaged aerodynamic roll and yaw torques acting on the robot body while in flight. The relative stroke-averaged aerodynamic forces between the right and left wings are given by

$$\Delta F_i \triangleq \int_0^T [\mathbf{F}_r(t) - \mathbf{F}_l(t)] \cdot \mathbf{e}_i^b dt, \quad i = 1, 2, 3 \quad (70)$$

For a positive sideslip angle β , both ΔF_1 and ΔF_3 decrease with increasing wind speed, as shown in Fig. 20, resulting in positive roll and yaw torques acting on the robot body. This phenomenon explains the coupling between roll and yaw motions observed in the lateral mode because any perturbation in the lateral velocity v_y induces a nonzero-sideslip angle that, in turn, generates restorative roll and yaw torques on the robot body.

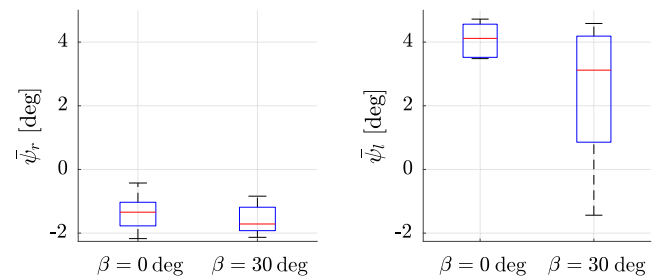


Fig. 19 Mean right- and left-wing pitch angles ($\bar{\psi}_r$ and $\bar{\psi}_l$) obtained from 10 trials conducted with a 0 deg sideslip angle, and then with a 30 deg sideslip angle, for a constant 0.5 m/s headwind.

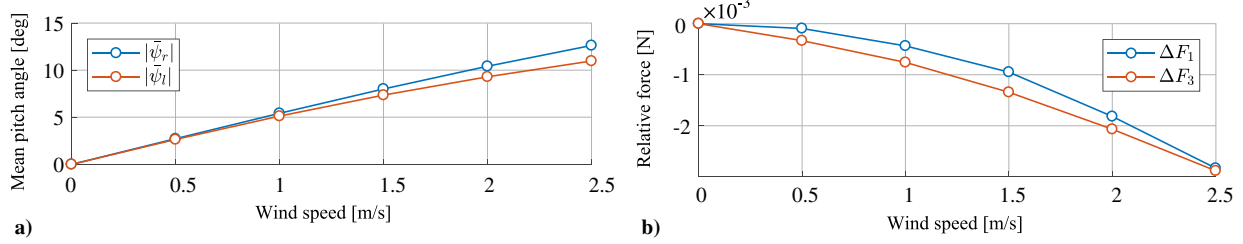


Fig. 20 Influence of increasing headwind velocity on a) wing mean pitch angle and b) resulting relative stroke-averaged aerodynamic forces between the two wings.

IX. Conclusions

Controlling insect-scale flapping-wing robots requires knowledge of the trim map and full flight envelope so as to account for asymmetrical command inputs and for the physical bounds afforded by the actuators. This paper presents an approach for deriving the nonlinear flight dynamic model of minimally actuated flapping-wing robots so as to capture the six degrees of freedom of the robot body and the degrees of freedom of each independent wing in a form amenable to set-point and flight envelope analysis. Because of the periodic nature of flapping flight, existing approaches for computing flight set points are not directly applicable to these robots. Therefore, command inputs corresponding to coordinated flapping turns and to longitudinal, lateral, and hovering flight are introduced and used to solve the equations of motion for steady and quasi-steady set-point conditions. A new approach is also presented for determining the full flight envelope of flapping-wing robots based on the robot dynamic model and on the dynamic actuator constraints imposed by the wing and hinge designs. The quasi-steady maneuvers and set points are used to identify and analyze dominant modes of motion and their stability in both numerical and physical experiments conducted on the RoboBee. As a result, the stability regions of the two dominant linear modes, referred to as longitudinal and lateral modes, are determined within the robot flight envelope. Furthermore, the time-domain specifications of the longitudinal and lateral modes and roll–yaw coupling effects observed in lateral flight are first determined numerically and then validated experimentally.

Appendix A: Yaw Control Through Shifted Mean Stroke Angles

The actuator dynamics described in Sec. III.A can be shown capable of controlling the robot yaw torque. This requires the wing pitch kinematics that govern ψ_r and ψ_l to be monotonic in the corresponding mean stroke angle ($\bar{\phi}_r$ and $\bar{\phi}_l$); thus, the actuator is designed to follow a stroke-plane trajectory such as Eq. (15). Under this assumption, a positive change to the mean stroke angle of both wings creates a positive yaw torque on the body by simultaneously creating a net positive aerodynamic force $\mathbf{F}_N(t)$ in the \mathbf{e}_1^b direction on the left wing and a net negative aerodynamic force on the right wing during a complete wing stroke. It can be shown that the integral of $\mathbf{F}_N(t)$ on the right wing in the \mathbf{e}_1^b direction over the total period T of a stroke is monotonic in the mean stroke angle, and a similar argument can be made for the left wing.

For the right wing, the average aerodynamic force in the \mathbf{e}_1^b direction over the course of a wing stroke is

$$F_1 \triangleq \int_0^{T/2} \mathbf{F}_N(t) \cdot \mathbf{e}_1^b dt + \int_{T/2}^T \mathbf{F}_N(t) \cdot \mathbf{e}_1^b dt \quad (\text{A1})$$

It can be shown that F_1 is a strictly decreasing function of $\bar{\phi}_r$ because

$$F_{1,d} \triangleq \int_0^{T/2} \mathbf{F}_N(t) \cdot \mathbf{e}_1^b dt$$

and

$$F_{1,u} \triangleq \int_{T/2}^T \mathbf{F}_N(t) \cdot \mathbf{e}_1^b dt$$

each are strictly decreasing functions of $\bar{\phi}_r$. It is convenient to split the wing stroke into the downstroke $\mathcal{T}_d = [0, T/2)$, during which the stroke angle $\phi_r(t) \in [-\pi/2, \pi/2]$ is strictly decreasing, and the upstroke $\mathcal{T}_u = [T/2, T)$, during which the stroke angle $\phi_r(t)$ is strictly increasing. For this analysis, assume hovering flight with zero body velocity.

Restricting the analysis to hovering flight, it is reasonable to assume that the wing pitch obeys the range $\psi_r(t) \in [-\pi/2, 0]$ for all $t \in \mathcal{T}_d$ and that $\psi_r(0) = \psi_r(T/2) = 0$. With these assumptions, the force $\mathbf{F}_N(t) \cdot \mathbf{e}_1^b$ is a strictly decreasing function of the angle of attack $\alpha_r \in [-\pi/2, \pi/2]$. For small stroke-plane deviations, the right-wing angle of attack can be approximated as

$$\alpha_r \approx -\text{atan}[\cos(\psi_r)/\sin(\psi_r)] = \psi_r + \pi/2, \quad \forall t \in \mathcal{T}_d \quad (\text{A2})$$

If ψ_r is a strictly decreasing function of $\bar{\phi}_r$, then, by extension, α_r is strictly decreasing in $\bar{\phi}_r$ for all $t \in \mathcal{T}_d$. Any positive changes to $\bar{\phi}_r$ will increase $F_{1,d}$ and any negative changes to $\bar{\phi}_r$ will decrease $F_{1,d}$ and $F_{1,u}$. Similarly for the upstroke, $F_{1,u}$ is a strictly decreasing function of $\bar{\phi}_r$. Assume now that $\psi_r(t) \in [0, \pi/2]$ for all $t \in \mathcal{T}_u$ and that $\psi_r(T/2) = \psi_r(T) = 0$. Under the small stroke-plane deviation assumption, the angle of attack during the upstroke is $\alpha_r \approx \psi_r - \pi/2$ for all $t \in \mathcal{T}_u$. If ψ_r is a strictly decreasing function of $\bar{\phi}_r$, then by extension, α_r is strictly decreasing in $\bar{\phi}_r$ for all $t \in \mathcal{T}_u$. Thus, $F_{1,u}$ is also a strictly decreasing function of $\bar{\phi}_r$, as is F_1 .

Appendix B: Kinematic Terms

The position vectors used in the equations of motion are

$$\mathbf{r}_{GA} = -d\mathbf{e}_3^b \quad (\text{B1})$$

$$\mathbf{r}_{AL} = l_1\mathbf{e}_2^l + h_1\mathbf{e}_3^l \quad (\text{B2})$$

$$\mathbf{r}_{AR} = l_1\mathbf{e}_2^r + h_1\mathbf{e}_3^r \quad (\text{B3})$$

where $d \in \mathbb{R}$, $l_1 \in \mathbb{R}$, and $h_1 \in \mathbb{R}$ are distance parameters determined from the robot geometry. The angular rates of the body, as well as the left and right wings with respect to the inertial frame, are

$$\boldsymbol{\omega}_b = \dot{\phi}\mathbf{e}_3^f + \dot{\theta}\mathbf{e}_1^{f'} + \dot{\psi}\mathbf{e}_2^b \quad (\text{B4})$$

$$\boldsymbol{\omega}_l = \dot{\phi}_l\mathbf{e}_3^b + \dot{\theta}_l\mathbf{e}_1^{l'} + \dot{\psi}_l\mathbf{e}_2^l + \boldsymbol{\omega}_b \quad (\text{B5})$$

$$\boldsymbol{\omega}_r = \dot{\phi}_r\mathbf{e}_3^b + \dot{\theta}_r\mathbf{e}_1^{r'} + \dot{\psi}_r\mathbf{e}_2^r + \boldsymbol{\omega}_b \quad (\text{B6})$$

where the basis vectors of the intermediate frames are $\mathbf{e}_1^f = \mathbf{R}(\mathbf{e}_3^f, \phi)\mathbf{e}_1^f$, $\mathbf{e}_1^l = \mathbf{R}(\mathbf{e}_3^b, \phi_1)\mathbf{e}_1^b$, and $\mathbf{e}_1^r = \mathbf{R}(\mathbf{e}_3^b, \phi)\mathbf{e}_1^b$. The rotation matrices, denoted with $\mathbf{R}(\cdot)$, are defined in Appendix C. The relative velocity vectors are obtained from the positions and angular rates of the corresponding rigid bodies:

$$\mathbf{v}_{GA} = \boldsymbol{\omega}_b \times \mathbf{r}_{GA} \quad (\text{B7})$$

$$\mathbf{v}_{AL} = \boldsymbol{\omega}_l \times \mathbf{r}_{AL} \quad (\text{B8})$$

$$\mathbf{v}_{AR} = \boldsymbol{\omega}_r \times \mathbf{r}_{AR} \quad (\text{B9})$$

Then, the accelerations of the body center of gravity G , the left-wing center of gravity L , and the right-wing center of gravity R can be written in terms of Eqs. (B1–B9) as follows:

$$\mathbf{a}_G = \ddot{\mathbf{x}}\mathbf{e}_1^f + \ddot{\mathbf{y}}\mathbf{e}_2^f + \ddot{\mathbf{z}}\mathbf{e}_3^f \quad (\text{B10})$$

$$\mathbf{a}_L = \mathbf{a}_G + \dot{\boldsymbol{\omega}}_b \times \mathbf{r}_{GA} + \boldsymbol{\omega}_b \times \mathbf{v}_{GA} + \dot{\boldsymbol{\omega}}_l \times \mathbf{r}_{AL} + \boldsymbol{\omega}_l \times \mathbf{v}_{AL} \quad (\text{B11})$$

$$\mathbf{a}_R = \mathbf{a}_G + \dot{\boldsymbol{\omega}}_b \times \mathbf{r}_{GA} + \boldsymbol{\omega}_b \times \mathbf{v}_{GA} + \dot{\boldsymbol{\omega}}_r \times \mathbf{r}_{AR} + \boldsymbol{\omega}_r \times \mathbf{v}_{AR} \quad (\text{B12})$$

Appendix C: Rotation Matrices

A rotation matrix $\mathbf{R} \in \text{SO}(3)$ can be computed from the axis of rotation represented by the unit vector $\mathbf{n} \in \mathbb{R}^3$ and from the angle of rotation $\eta \in [0, 2\pi)$:

$$\mathbf{R}(\mathbf{n}, \eta) \triangleq [1 - \cos(\eta)]\mathbf{nn}^T + \cos(\eta)\mathbf{I}_3 + \sin(\eta)\mathbf{S}(\mathbf{n}) \quad (\text{C1})$$

where $\mathbf{I}_3 \in \mathbb{R}^{3 \times 3}$ is the identity matrix, and $\mathbf{S}(\mathbf{n})$ denotes the skew-symmetric matrix

$$\mathbf{S}(\mathbf{n}) \triangleq \begin{bmatrix} 0 & -n_3 & n_2 \\ n_3 & 0 & -n_1 \\ -n_2 & n_1 & 0 \end{bmatrix} \quad (\text{C2})$$

obtained from $\mathbf{n} = [n_1 \ n_2 \ n_3]^T$.

Acknowledgment

This work was supported by the Office of Naval Research grant N00014-17-1-2614.

References

- [1] Whitney, J. P., Sreetharan, P. S., Ma, K. Y., and Wood, R. J., "Pop-Up Book MEMS," *Journal of Micromechanics and Microengineering*, Vol. 21, No. 11, 2011, Paper 115021. <https://doi.org/10.1088/0960-1317/21/11/115021>
- [2] Ma, K. Y., Felton, S. M., and Wood, R. J., "Design, Fabrication, and Modeling of the Split Actuator Microrobotic Bee," *2012 IEEE/RSJ International Conference on Intelligent Robots and Systems*, Inst. of Electrical and Electronics Engineers, New York, 2012, pp. 1133–1140. <https://doi.org/10.1109/IROS.2012.6386192>
- [3] Jafferis, N. T., Smith, M. J., and Wood, R. J., "Design and Manufacturing Rules for Maximizing the Performance of Polycrystalline Piezoelectric Bending Actuators," *Smart Materials and Structures*, Vol. 24, No. 6, 2015, Paper 065023. <https://doi.org/10.1088/0964-1726/24/6/065023>
- [4] Jafferis, N. T., Lok, M., Winey, N., Wei, G.-Y., and Wood, R. J., "Multilayer Laminated Piezoelectric Bending Actuators: Design and Manufacturing for Optimum Power Density and Efficiency," *Smart Materials and Structures*, Vol. 25, No. 5, 2016, Paper 055033. <https://doi.org/10.1088/0964-1726/25/5/055033>
- [5] Cox, A., Monopoli, D., Cveticanin, D., Goldfarb, M., and Garcia, E., "The Development of Elastodynamic Components for Piezoelectrically Actuated Flapping Micro-Air Vehicles," *Journal of Intelligent Material Systems and Structures*, Vol. 13, No. 9, 2002, pp. 611–615. <https://doi.org/10.1106/104538902032463>
- [6] Anderson, M. L., "Design and Control of Flapping Wing Micro Air Vehicles," Air Force Inst. of Technology TR AFIT/DS/ENY/11-1, School of Engineering and Management, Wright–Patterson AFB, OH, 2011.
- [7] Finio, B. M., Pérez-Arancibia, N. O., and Wood, R. J., "System Identification and Linear Time-Invariant Modeling of an Insect-Sized Flapping-Wing Micro Air Vehicle," *2011 IEEE/RSJ International Conference on Intelligent Robots and Systems (IROS)*, Inst. of Electrical and Electronics Engineers, New York, 2011, pp. 1107–1114. <https://doi.org/10.1109/IROS.2011.6094421>
- [8] Hines, L., Campolo, D., and Sitti, M., "Lift-off of a Motor-Driven, Flapping-Wing Microaerial Vehicle Capable of Resonance," *IEEE Transactions on Robotics*, Vol. 30, No. 1, 2014, pp. 220–232. <https://doi.org/10.1109/TRO.2013.2280057>
- [9] Floreano, D., and Wood, R. J., "Science, Technology and the Future of Small Autonomous Drones," *Nature*, Vol. 521, No. 7553, 2015, Paper 460. <https://doi.org/10.1038/nature14542>
- [10] Helbling, E. F., and Wood, R. J., "A Review of Propulsion, Power, and Control Architectures for Insect-Scale Flapping-Wing Vehicles," *Applied Mechanics Reviews*, Vol. 70, No. 1, 2018, Paper 010801. <https://doi.org/10.1115/1.4038795>
- [11] Haldane, J. B. S., "On Being the Right Size," *Harper's Magazine*, Vol. 152, 1926, pp. 424–427.
- [12] Jayaram, K. et al., "Transition by Head-On Collision: Mechanically Mediated Manoeuvres in Cockroaches and Small Robots," *Journal of the Royal Society Interface*, Vol. 15, No. 139, 2018, Paper 20170664.
- [13] Clawson, T. S., Ferrari, S., Fuller, S. B., and Wood, R. J., "Spiking Neural Network (SNN) Control of a Flapping Insect-Scale Robot," *2016 IEEE 55th Conference on Decision and Control (CDC)*, Inst. of Electrical and Electronics Engineers, New York, 2016, pp. 3381–3388. <https://doi.org/10.1109/CDC.2016.7798778>
- [14] Clawson, T. S., Stewart, T. C., Eliasmith, C., and Ferrari, S., "An Adaptive Spiking Neural Controller for Flapping Insect-Scale Robots," *2017 IEEE Symposium Series on Computational Intelligence (SSCI)*, Inst. of Electrical and Electronics Engineers, New York, 2017, pp. 1–7. <https://doi.org/10.1109/SSCI.2017.8285173>
- [15] Doman, D. B., Oppenheimer, M. W., and Sigthorsson, D. O., "Wingbeat Shape Modulation for Flapping-Wing Micro-Air-Vehicle Control During Hover," *Journal of Guidance, Control, and Dynamics*, Vol. 33, No. 3, 2010, pp. 724–739. <https://doi.org/10.2514/1.47146>
- [16] Oppenheimer, M. W., Doman, D. B., and Sigthorsson, D. O., "Dynamics and Control of a Biomimetic Vehicle Using Biased Wingbeat Forcing Functions," *Journal of Guidance, Control, and Dynamics*, Vol. 34, No. 1, 2011, pp. 204–217. <https://doi.org/10.2514/1.49735>
- [17] Oppenheimer, M. W., Weintraub, I. E., Sigthorsson, D. O., and Doman, D. B., "Control of a Minimally Actuated Biomimetic Vehicle Using Quarter-Cycle Wingbeat Modulation," *Journal of Guidance, Control, and Dynamics*, Vol. 38, No. 7, 2015, pp. 1187–1196. <https://doi.org/10.2514/1.G000548>
- [18] Chirarattananon, P., Ma, K. Y., and Wood, R. J., "Adaptive Control of a Millimeter-Scale Flapping-Wing Robot," *Bioinspiration and Biomimetics*, Vol. 9, No. 2, 2014, Paper 025004. <https://doi.org/10.1088/1748-3182/9/2/025004>
- [19] Chirarattananon, P., Chen, Y., Helbling, E. F., Ma, K. Y., Cheng, R., and Wood, R. J., "Dynamics and Flight Control of a Flapping-Wing Robotic Insect in the Presence of Wind Gusts," *Interface Focus*, Vol. 7, No. 1, 2017, Paper 20160080. <https://doi.org/10.1098/rsfs.2016.0080>
- [20] Deng, X., Schenato, L., and Sastry, S. S., "Flapping Flight for Biomimetic Robotic Insects: Part II-Flight Control Design," *IEEE Transactions on Robotics*, Vol. 22, No. 4, 2006, pp. 789–803. <https://doi.org/10.1109/TRO.2006.875483>
- [21] Dickson, W. B., Straw, A. D., Poelma, C., and Dickinson, M. H., "An Integrative Model of Insect Flight Control," *44th AIAA Aerospace Sciences Meeting and Exhibit*, AIAA Paper 2006-0034, 2006. <https://doi.org/10.2514/6.2006-34>
- [22] Gallagher, J. C., Doman, D. B., and Oppenheimer, M. W., "The Technology of the Gaps: An Evolvable Hardware Synthesized Oscillator for the Control of a Flapping-Wing Micro Air Vehicle," *IEEE Transactions on Evolutionary Computation*, Vol. 16, No. 6, 2012, pp. 753–768. <https://doi.org/10.1109/TEVC.2012.2186816>
- [23] Biswal, S., Mignolet, M., and Rodriguez, A., "Modeling and Control of Flapping Wing Micro Aerial Vehicles," *Bioinspiration and Biomimetics*, Vol. 14, No. 2, 2019, Paper 026004. <https://doi.org/10.1088/1748-3190/aafc3c>
- [24] Taha, H. E., Woolsey, C. A., and Hajj, M. R., "Geometric Control Approach to Longitudinal Stability of Flapping Flight," *Journal*

- of *Guidance, Control, and Dynamics*, Vol. 39, No. 2, 2015, pp. 214–226.
<https://doi.org/10.2514/1.G001280>
- [25] Taha, H. E., Tahmasian, S., Woolsey, C. A., Nayfeh, A. H., and Hajj, M. R., “The Need for Higher-Order Averaging in the Stability Analysis of Hovering, Flapping-Wing Flight,” *Bioinspiration and Biomimetics*, Vol. 10, No. 1, 2015, Paper 016002.
<https://doi.org/10.1088/1748-3190/10/1/016002>
- [26] Serrani, A., “Robust Nonlinear Control Design for a Minimally-Actuated Flapping-Wing MAV in the Longitudinal Plane,” *2011 50th IEEE Conference on Decision and Control and European Control Conference*, Inst. of Electrical and Electronics Engineers, New York, 2011, pp. 7464–7469.
<https://doi.org/10.1109/CDC.2011.6160856>
- [27] Stengel, R. F., *Flight Dynamics*, Princeton Univ. Press, Princeton, NJ, 2015.
<https://doi.org/10.2307/j.ctt1287kgx>
- [28] Stengel, R. F., *Optimal Control and Estimation*, Courier Corp., Chelmsford, MA, 2012.
- [29] Nelson, R. C., *Flight Stability and Automatic Control*, Vol. 2, WCB/McGraw-Hill, New York, 1998.
<https://doi.org/10.1017/S0001924000065362>
- [30] Ferrari, S., and Stengel, R. F., “Online Adaptive Critic Flight Control,” *Journal of Guidance, Control, and Dynamics*, Vol. 27, No. 5, 2004, pp. 777–786.
<https://doi.org/10.2514/1.12597>
- [31] Ferrari, S., and Stengel, R. F., “An Adaptive Critic Global Controller,” *Proceedings of the 2002 American Control Conference (IEEE Cat. No. CH37301)*, Vol. 4, Inst. of Electrical and Electronics Engineers, New York, 2002, pp. 2665–2670.
- [32] Ferrari, S., and Jensenius, M., “Robust and Reconfigurable Flight Control by Neural Networks,” *Infotech@Aerospace*, AIAA Paper 2005-7037, 2005.
- [33] Ferrari, S., “Algebraic and Adaptive Learning in Neural Control Systems,” Ph.D. Thesis, Dept. of Mechanical and Aerospace Engineering, Princeton Univ., Princeton, NJ, 2002.
- [34] Chandramohan, R., Steck, J., Rokhsaz, K., and Ferrari, S., “Adaptive Critic Flight Control for a General Aviation Aircraft: Simulations for the Beech Bonanza Fly-by-Wire Test Bed,” *AIAA Infotech@Aerospace 2007 Conference and Exhibit*, AIAA Paper 2007-2795, 2007.
- [35] Ferrari, S., Steck, J. E., and Chandramohan, R., “Adaptive Feedback Control by Constrained Approximate Dynamic Programming,” *IEEE Transactions on Systems, Man, and Cybernetics, Part B (Cybernetics)*, Vol. 38, No. 4, 2008, pp. 982–987.
- [36] Ferrari, S., and Stengel, R. F., “Classical/Neural Synthesis of Nonlinear Control Systems,” *Journal of Guidance, Control, and Dynamics*, Vol. 25, No. 3, 2002, pp. 442–448.
- [37] Chang, S., and Wang, Z. J., “Predicting Fruit Fly’s Sensing Rate with Insect Flight Simulations,” *Proceedings of the National Academy of Sciences*, Vol. 111, No. 31, 2014, pp. 11246–11251.
<https://doi.org/10.1073/pnas.1314738111>
- [38] Orlowski, C. T., and Girard, A. R., “Modeling and Simulation of Nonlinear Dynamics of Flapping Wing Micro Air Vehicles,” *AIAA Journal*, Vol. 49, No. 5, 2011, pp. 969–981.
<https://doi.org/10.2514/1.J050649>
- [39] Doman, D., Oppenheimer, M., and Sigthorsson, D., “Dynamics and Control of a Minimally Actuated Biomimetic Vehicle: Part I—Aerodynamic Model,” *AIAA Guidance, Navigation, and Control Conference*, AIAA Paper 2009-6160, 2009.
<https://doi.org/10.2514/6.2009-6160>
- [40] Clawson, T. S., Fuller, S. B., Wood, R. J., and Ferrari, S., “A Blade Element Approach to Modeling Aerodynamic Flight of an Insect-Scale Robot,” *American Control Conference (ACC)*, Inst. of Electrical and Electronics Engineers, New York, 2017, pp. 2843–2849.
<https://doi.org/10.23919/ACC.2017.7963382>
- [41] Sun, M., “Insect Flight Dynamics: Stability and Control,” *Reviews of Modern Physics*, Vol. 86, No. 2, 2014, Paper 615.
<https://doi.org/10.1103/RevModPhys.86.615>
- [42] Xu, N., and Sun, M., “Lateral Dynamic Flight Stability of a Model Bumblebee in Hovering and Forward Flight,” *Journal of Theoretical Biology*, Vol. 319, Feb. 2013, pp. 102–115.
<https://doi.org/10.1016/j.jtbi.2012.11.033>
- [43] Wu, J. H., and Sun, M., “Floquet Stability Analysis of the Longitudinal Dynamics of Two Hovering Model Insects,” *Journal of the Royal Society Interface*, Vol. 9, No. 74, 2012, pp. 2033–2046.
<https://doi.org/10.1098/rsif.2012.0072>
- [44] Liang, B., and Sun, M., “Nonlinear Flight Dynamics and Stability of Hovering Model Insects,” *Journal of the Royal Society Interface*, Vol. 10, No. 85, 2013, Paper 20130269.
<https://doi.org/10.1098/rsif.2013.0269>
- [45] Sun, M., and Xiong, Y., “Dynamic Flight Stability of a Hovering Bumblebee,” *Journal of Experimental Biology*, Vol. 208, No. 3, 2005, pp. 447–459.
<https://doi.org/10.1242/jeb.01407>
- [46] Zhang, Y., and Sun, M., “Dynamic Flight Stability of a Hovering Model Insect: Lateral Motion,” *Acta Mechanica Sinica*, Vol. 26, No. 2, 2010, pp. 175–190.
<https://doi.org/10.1007/s10409-009-0303-1>
- [47] Ristroph, L., Ristroph, G., Morozova, S., Bergou, A. J., Chang, S., Guckenheimer, J., Wang, Z. J., and Cohen, I., “Active and Passive Stabilization of Body Pitch in Insect Flight,” *Journal of the Royal Society Interface*, Vol. 10, No. 85, 2013, Paper 20130237.
<https://doi.org/10.1098/rsif.2013.0237>
- [48] Cheng, B., and Deng, X., “Translational and Rotational Damping of Flapping Flight and Its Dynamics and Stability at Hovering,” *IEEE Transactions on Robotics*, Vol. 27, No. 5, 2011, pp. 849–864.
<https://doi.org/10.1109/TRO.2011.2156170>
- [49] Hedrick, T. L., Cheng, B., and Deng, X., “Wingbeat Time and the Scaling of Passive Rotational Damping in Flapping Flight,” *Science*, Vol. 324, No. 5924, 2009, pp. 252–255.
<https://doi.org/10.1126/science.1168431>
- [50] Xiong, Y., and Sun, M., “Dynamic Flight Stability of a Bumblebee in Forward Flight,” *Acta Mechanica Sinica*, Vol. 24, No. 1, 2008, pp. 25–36.
<https://doi.org/10.1007/s10409-007-0121-2>
- [51] Faruque, I., MacFarlane, K., and Humbert, J., “Reduced-Order Forward Flight Dynamics Models for Dipteran Insects,” *AIAA Guidance, Navigation, and Control Conference*, AIAA Paper 2012-4978, 2012.
<https://doi.org/10.2514/6.2012-4978>
- [52] Taha, H., and Hajj, M., “Unsteady Nonlinear Aerodynamics of Hovering Mavs/Insects,” *51st AIAA Aerospace Sciences Meeting Including the New Horizons Forum and Aerospace Exposition*, AIAA Paper 2013-0504, 2013.
<https://doi.org/10.2514/6.2013-504>
- [53] Taha, H. E., Hajj, M. R., and Beran, P. S., “State-Space Representation of the Unsteady Aerodynamics of Flapping Flight,” *Aerospace Science and Technology*, Vol. 34, April 2014, pp. 1–11.
<https://doi.org/10.1016/j.ast.2014.01.011>
- [54] Wang, Z. J., Birch, J. M., and Dickinson, M. H., “Unsteady Forces and Flows in Low Reynolds Number Hovering Flight: Two-Dimensional Computations vs Robotic Wing Experiments,” *Journal of Experimental Biology*, Vol. 207, No. 3, 2004, pp. 449–460.
<https://doi.org/10.1242/jeb.00739>
- [55] Wang, Z. J., “Two Dimensional Mechanism for Insect Hovering,” *Physical Review Letters*, Vol. 85, No. 10, 2000, pp. 2216–2219.
<https://doi.org/10.1103/PhysRevLett.85.2216>
- [56] Ma, K. Y., Chirarattananon, P., Fuller, S. B., and Wood, R. J., “Controlled Flight of a Biologically Inspired, Insect-Scale Robot,” *Science*, Vol. 340, No. 6132, 2013, pp. 603–607.
<https://doi.org/10.1126/science.1231806>
- [57] Finio, B. M., and Wood, R. J., “Open-Loop Roll, Pitch and Yaw Torques for a Robotic Bee,” *2012 IEEE/RSJ International Conference on Intelligent Robots and Systems (IROS)*, Inst. of Electrical and Electronics Engineers, New York, 2012, pp. 113–119.
<https://doi.org/10.1109/IROS.2012.6385519>
- [58] Hines, L. L., Arabagi, V., and Sitti, M., “Free Flight Simulations and Pitch and Roll Control Experiments of a Sub-Gram Flapping-Flight Micro Aerial Vehicle,” *2011 IEEE International Conference on Robotics and Automation*, IEEE, New York, 2011, pp. 1–7.
- [59] Steltz, E., Wood, R. J., Avadhanula, S., and Fearing, R. S., “Characterization of the Micromechanical Flying Insect by Optical Position Sensing,” *Proceedings of the 2005 IEEE International Conference on Robotics and Automation, ICRA 2005*, Inst. of Electrical and Electronics Engineers, New York, 2005, pp. 1252–1257.
<https://doi.org/10.1109/ROBOT.2005.1570287>
- [60] James, J., Iyer, V., Chukewad, Y., Gollakota, S., and Fuller, S. B., “Liftoff of a 190 Mg Laser-Powered Aerial Vehicle: The Lightest Wire-less Robot to Fly,” *2018 IEEE International Conference on Robotics and Automation (ICRA)*, Inst. of Electrical and Electronics Engineers, New York, 2018, pp. 1–8.
<https://doi.org/10.1109/ICRA.2018.8460582>
- [61] Zou, Y., Zhang, W., and Zhang, Z., “Liftoff of an Electromagnetically Driven Insect-Inspired Flapping-Wing Robot,” *IEEE Transactions on Robotics*, Vol. 32, No. 5, 2016, pp. 1285–1289.
<https://doi.org/10.1109/TRO.2016.2593449>
- [62] Richter, C., and Lipson, H., “Untethered Hovering Flapping Flight of a 3D-Printed Mechanical Insect,” *Artificial Life*, Vol. 17, No. 2,

- 2011, pp. 73–86.
https://doi.org/10.1162/artl_a_00020
- [63] Rosen, M. H., le Pivain, G., Sahai, R., Jafferis, N. T., and Wood, R. J., “Development of a 3.2 g Untethered Flapping-Wing Platform for Flight Energetics and Control Experiments,” *2016 IEEE International Conference on Robotics and Automation (ICRA)*, Inst. of Electrical and Electronics Engineers, New York, 2016, pp. 3227–3233.
<https://doi.org/10.1109/ICRA.2016.7487492>
- [64] Oppenheimer, M. W., Sigthorsson, D., Doman, D. B., and Weintraub, I., “Wing Design and Testing for a Tailless Flapping Wing Micro-Air Vehicle,” *AIAA Guidance, Navigation, and Control Conference*, AIAA Paper 2017-1271, 2017.
<https://doi.org/10.2514/6.2017-1271>
- [65] Deng, X., Schenato, L., Wu, W. C., and Sastry, S. S., “Flapping Flight for Biomimetic Robotic Insects: Part I-System Modeling,” *IEEE Transactions on Robotics*, Vol. 22, No. 4, 2006, pp. 776–788.
<https://doi.org/10.1109/TRO.2006.875480>
- [66] Dickson, W. B., Straw, A. D., and Dickinson, M. H., “Integrative Model of Drosophila Flight,” *AIAA Journal*, Vol. 46, No. 9, 2008, pp. 2150–2164.
- [67] Ferrari, S., and Stengel, R. F., “Smooth Function Approximation Using Neural Networks,” *IEEE Transactions on Neural Networks*, Vol. 16, No. 1, 2005, pp. 24–38.
- [68] Rowley, C. W., and Dawson, S. T., “Model Reduction for Flow Analysis and Control,” *Annual Review of Fluid Mechanics*, Vol. 49, Jan. 2017, pp. 387–417.
<https://doi.org/10.1146/annurev-fluid-010816-060042>
- [69] Kutz, J. N., Brunton, S. L., Brunton, B. W., and Proctor, J. L., *Dynamic Mode Decomposition: Data-Driven Modeling of Complex Systems*, Vol. 149, Soc. for Industrial and Applied Mathematics, Philadelphia, 2016.
<https://doi.org/10.1137/1.9781611974508.bm>
- [70] Taha, H. E., Nayfeh, A. H., and Hajj, M. R., “Effect of the Aerodynamic-Induced Parametric Excitation on the Longitudinal Stability of Hovering MAVs/Insects,” *Nonlinear Dynamics*, Vol. 78, No. 4, 2014, pp. 2399–2408.
- [71] Dickinson, M. H., Lehmann, F.-O., and Sane, S. P., “Wing Rotation and the Aerodynamic Basis of Insect Flight,” *Science*, Vol. 284, No. 5422, 1999, pp. 1954–1960.
<https://doi.org/10.1126/science.284.5422.1954>
- [72] Doman, D., Oppenheimer, M., Sigthorsson, D., Weintraub, I., and Perseghetti, B., “Wing Velocity Control System for Testing Body Motion Control Methods for Flapping Wing MAVs,” *51st AIAA Aerospace Sciences Meeting Including the New Horizons Forum and Aerospace Exposition*, AIAA Paper 2013-0332, 2013.
<https://doi.org/10.2514/6.2013-332>
- [73] Sigthorsson, D., Oppenheimer, M. W., Doman, D. B., and Weintraub, I., “Wing Flexibility Induced Control Reversal for Flapping Wing Vehicles: Observation and Evaluation,” *AIAA Guidance, Navigation, and Control Conference*, AIAA Paper 2017-1273, 2017.
<https://doi.org/10.2514/6.2017-1273>
- [74] Ristroph, L., Berman, G. J., Bergou, A. J., Wang, Z. J., and Cohen, I., “Automated Hull Reconstruction Motion Tracking (HRMT) Applied to Sideways Maneuvers of Free-Flying Insects,” *Journal of Experimental Biology*, Vol. 212, No. 9, 2009, pp. 1324–1335.
<https://doi.org/10.1242/jeb.025502>
- [75] Zhang, J., and Deng, X., “Resonance Principle for the Design of Flapping Wing Micro Air Vehicles,” *IEEE Transactions on Robotics*, Vol. 33, No. 1, 2017, pp. 183–197.
<https://doi.org/10.1109/TRO.2016.2626457>
- [76] Ellington, C. P., “The Novel Aerodynamics of Insect Flight: Applications to Micro-Air Vehicles,” *Journal of Experimental Biology*, Vol. 202, No. 23, 1999, pp. 3439–3448.
- [77] Sun, M., and Tang, J., “Unsteady Aerodynamic Force Generation by a Model Fruit Fly Wing in Flapping Motion,” *Journal of Experimental Biology*, Vol. 205, No. 1, 2002, pp. 55–70.
- [78] Andersen, A., Pesavento, U., and Wang, Z. J., “Unsteady Aerodynamics of Fluttering and Tumbling Plates,” *Journal of Fluid Mechanics*, Vol. 541, Oct. 2005, pp. 65–90.
<https://doi.org/10.1017/S002211200500594X>
- [79] Nakata, T., Liu, H., and Bompfrey, R. J., “A CFD-Informed Quasi-Steady Model of Flapping-Wing Aerodynamics,” *Journal of Fluid Mechanics*, Vol. 783, Nov. 2015, pp. 323–343.
<https://doi.org/10.1017/jfm.2015.537>
- [80] Sane, S. P., and Dickinson, M. H., “The Control of Flight Force by a Flapping Wing: Lift and Drag Production,” *Journal of Experimental Biology*, Vol. 204, No. 15, 2001, pp. 2607–2626.
- [81] Whitney, J., and Wood, R., “Aeromechanics of Passive Rotation in Flapping Flight,” *Journal of Fluid Mechanics*, Vol. 660, Oct. 2010, pp. 197–220.
<https://doi.org/10.1017/S002211201000265X>
- [82] Betts, J. T., *Practical Methods for Optimal Control and Estimation Using Nonlinear Programming*, Soc. for Industrial and Applied Mathematics, Philadelphia, 2010.
<https://doi.org/10.1137/1.9780898718577>
- [83] Clawson, T., “Neuromorphic Sensing and Control of Autonomous Micro-Aerial Vehicles,” Ph.D. Thesis, Sibley School of Mechanical and Aerospace Engineering, Cornell Univ., Ithaca, NY, 2019.